Influence of Continental Geometry on the Onset and Spatial Distribution of Monsoonal Precipitation

Katrina L. Hui*

Environmental Science and Engineering, California Institute of Technology, Pasadena, California

Simona Bordoni

Department of Civil, Environmental and Mechanical Engineering, University of Trento, 38123 Trento, Italy

Environmental Science and Engineering, California Institute of Technology, Pasadena, CA

**Corresponding author address:* Katrina L. Hui, California Institute of Technology, 1200 E. California Blvd., Pasadena, CA 91125.

E-mail: klhui@caltech.edu

ABSTRACT

Recent studies have shown that the rapid onset of the monsoon can be interpreted as a switch in the tropical circulation, which can occur even in the absence of land-sea contrast, between a dynamical regime controlled by eddy momentum fluxes to a monsoon regime more directly controlled by energetic constraints. Here we investigate the influence of continental geometry on such transitions. We conduct experiments with an aquaplanet model with a slab ocean, in which different zonally symmetric continents are prescribed in the Northern Hemisphere poleward from southern boundaries at various latitudes, with "land" having a mixed layer depth two orders of magnitude smaller than ocean. For continents extending to tropical latitudes, the simulated monsoon features a rapid migration of the convergence zone over the continent, similar to what is seen in the Asian monsoon. For continents with more poleward southern boundaries, the main precipitation zone remains over the ocean, moving gradually into the summer hemisphere. We show that the absence of land at tropical latitudes prevents the establishment of a reversed meridional gradient in lower-level moist static energy and, with it, an overturning circulation with poleward displaced convergence zone that can transition rapidly into an angular momentum conserving monsoon regime. Implications for observed monsoons are discussed.

1. Introduction

The monsoon is a prominent climatological phenomenon of the summertime circulation that dominates the annual cycle over much of the tropics and subtropics. It brings abundant rainfall to regions that feature otherwise very arid winters, so its onset, strength, and variability have large socioeconomic impacts. All regional monsoons are characterized by rainfall largely confined in the warm season, with accompanying circulation changes. However, each monsoon can differ in its strength, extent, and onset timing depending on factors such as topography and continental geometry. While recent work suggests that land-sea contrast is not necessary to generate monsoons (Bordoni and Schneider 2008), there is no doubt that the land-sea distribution influences these systems in important ways, which motivates investigations of the influence of continental geometry on the monsoon timing and strength (Dirmeyer 1998; Xie and Saiki 1999; Chou et al. 2001).

Over the past two decades, understanding has emerged and led to novel consideration of monsoons as intimately tied to the tropical overturning circulation and associated Intertropical Convergence Zone (ITCZ). In fact, monsoons are now widely viewed as broad, cross-equatorial Hadley circulations that are energetically direct and export energy away from their ascending branches (e.g., Biasutti et al. 2018) and that project strongly on the global zonal mean (e.g., Walker and Bordoni 2016; Walker 2017). According to this emerging view, monsoons are a manifestation of the seasonal excursion of the ITCZ into the summer hemisphere subtropical continents. In this respect, theories that have been developed for the understanding of the Hadley cell and its response to perturbations by different forcings and on different timescales might be applicable, at least to some extent, to the understanding of monsoons.

There is a rich history in using axisymmetric models to study the Hadley circulation using constraints provided by the angular momentum (AM) budget. Although axisymmetric theory is idealized, as it neglects effects of viscosity and eddies, it is able to elegantly produce tropical circulations similar to those observed using concepts of AM and energy conservation (Held and Hou 1980; Lindzen and Hou 1988; Plumb and Hou 1992; Privé and Plumb 2007a). One important limitation of the dry framework with a prescribed radiative equilibrium temperature distribution often used in these studies (Held and Hou 1980; Lindzen and Hou 1988; Plumb and Hou 1992) is that it unrealistically prevents the induced circulation from interacting with and influencing the thermal forcing field. Also, nonlinear axisymmetric models take much longer to reach steady state than the seasonal timescale associated with the transient monsoon, raising questions on the applicability of their results to seasonally evolving circulations. To address these limitations, studies have progressively included the effects of extratropical eddies, which influence the energy and momentum transport in the extratropics in ways that have been shown to be nontrivial for steady Hadley circulations (Walker and Schneider 2006). In simulations with idealized general circulation models (GCM) with a seasonal cycle and no zonal asymmetries, Schneider and Bordoni (2008) and Bordoni and Schneider (2008) showed that the rapid onset of the monsoon might be interpreted as a switch between a dynamical regime where the tropical circulation strength is controlled by eddy momentum fluxes and a monsoon regime where the strength is more directly controlled by energetic constraints, which causes the monsoonal cross-equatorial cell to grow rapidly in strength and extent. This switch can happen even in the absence of surface inhomogeneities, provided that the lower boundary has low enough thermal inertia. More recently, work by Geen et al. (2018) provides a complimentary view to the AM budget by focusing on the vorticity budget and finding that this transition can also be thought of as a rapid reduction in the upper-level absolute vorticity within the tropical circulation due to positive horizontal advection and negative vortex stretching tendencies.

An alternative framework that has also allowed for significant progress in the understanding of the zonally averaged Hadley cell and the ITCZ has been based on the atmospheric energy budget, which interprets the ITCZ response as part of the meridional energy fluxes necessary to restore energy balance to a given perturbation (Kang et al. 2008; Bischoff and Schneider 2014). While the extension of this framework to zonally asymmetric circulations, such as monsoons, remains an area of active research (e.g., Boos and Korty 2016; Adam et al. 2016), constraints that apply to the zonal mean could also prove useful to regional monsoons (e.g., Schneider et al. 2014). See Hill (2019) for a review of merits of and outstanding challenges in energy-based theories of monsoons.

In this work, we want to understand how simple aspects of continental geometry influence the fundamental dynamics of monsoonal circulations building on more idealized work. As argued by recent studies (Jeevanjee et al. 2017; Collins et al. 2018), approaches in which complexity is increased progressively allow for understanding of fundamental dynamics in the absence of other complicating but poorly understood factors. Expanding on the work of Bordoni and Schneider (2008), we introduce continents with very idealized geometry in an otherwise aquaplanet lower boundary in a GCM with idealized physics. Similar approaches were taken in models with more realistic physics (e.g., Dirmeyer 1998; Xie and Saiki 1999; Chou et al. 2001). Here we attempt to fill the gap between idealized aquaplanet GCMs and comprehensive models. This study is also similar in spirit to the goals of the Tropical Rain belts with an Annual cycle and a Continent Model Intercomparison Project (TRACMIP, Voigt et al. 2016), but here we focus on just one model and study the response of monsoons to changes in one aspect of continental configuration (position of the equatorward coastal boundary).

As demonstrated in Figure 1, the various monsoon systems around the world have different spatial extent. They also feature different monsoon season lengths; what controls the timing of monsoon onset is not well understood, especially in terms of its year-to-year variability in different regions. Here, we want to address the more fundamental question of how the different distribution of land masses around the near-equatorial region might explain differences in the climatology of the onset timing and spatial distribution of monsoonal rainfall. We use a three-dimensional idealized GCM that includes important processes for the monsoon, such as seasonality and large-scale eddies. We aim to concentrate on simple aspects of continental geometry by focusing on the effects of land-ocean heat capacity contrast and removing surface land hydrology, land-sea albedo contrasts, and topography. We expand on the work by Laraia (2015) and run the model with five different zonally symmetric configurations of Northern Hemisphere (NH) land that extends poleward from southern boundaries at various latitudes to vary the hemispheric asymmetry in thermal inertia. We interpret the development of monsoons as the seasonal migration of the ITCZ into subtropical latitudes, and we study how it is impacted, together with accompanying circulation changes, by changes in continental configuration. Section 2 describes the idealized GCM and simulations used in this study, as well as the monsoon onset indices and data used for comparison to observations. Section 3 focuses on the seasonal cycle of precipitation in the different experiments, and Section 4 interprets these results using dynamical constraints. A discussion of the relationship of our work to previous work is included in Section 5. Finally, conclusions and future work are summarized in Section 6.

2. Methods and Tools

a. Idealized GCM

A moist idealized aquaplanet GCM based on the Geophysical Fluid Dynamics Laboratory (GFDL) Flexible Modeling System (Frierson et al. 2006; O'Gorman and Schneider 2008) is used, which solves the primitive equations of motion on a sphere with the Earth's radius.

The lower boundary of the model consists of a slab ocean, whose sea surface temperatures (T_s) evolve according to the surface energy budget:

$$c\rho d\frac{\partial T_s}{\partial t} = O_s = S^s - L^s - LH - SH - \nabla \cdot F_0, \tag{1}$$

which states that ocean heat storage O_s on the left hand side, with water specific heat c, density ρ, and mixed layer depth d, is balanced by radiative and turbulent energy fluxes into the surface (with net incoming shortwave flux S^s, net outgoing longwave flux L^s, outgoing sensible SH and latent LH heat fluxes) and any energy flux convergence ($-\nabla \cdot F_0$) by ocean currents. In our simulations, land and ocean only differ in the corresponding mixed layer depth d, which we choose as 0.2 m for land and 20 m for ocean. The surface albedo is spatially uniform and fixed at an Earth-like value of $\alpha = 0.38$. A two-stream grey radiation scheme is used where the optical depth is prescribed. While a diurnal cycle is not included, the GCM is forced by a seasonal cycle of insolation with a 360-day Julian year, using realistic Earth-like values of obliquity and solar constant of $23.5°$ and 1360 W m^{-2} respectively, but zero eccentricity. The GCM includes an active hydrological cycle, where precipitation can form by either large-scale condensation or convection following a simplified Betts-Miller convection scheme as in Frierson (2007). Since precipitation is assumed to fall out immediately, there is no liquid water or ice in the atmosphere, hence no clouds. With these simplifications, this GCM does not account for important climate feedbacks such as surface albedo, cloud, or radiative water vapor feedbacks, but nonetheless well resolves tropical and extratropical circulations, their mutual interactions, and their impact on the hydrological cycle.

For this study, we performed five simulations with an idealized continent. The model is run with fully saturated NH land ($d = 0.2$ m) that extends poleward from southern boundaries at 0°, 10°, 20°, 30°, and 40° (Fig. 2a), with ocean mixed layer depth $d = 20$ m. One aquaplanet simulation was also run with all ocean ($d = 20$ m everywhere). For each simulation, the ocean energy transport is prescribed through the ocean Q flux term in Eq. (1) following the zonally symmetric and time-invariant form in Merlis et al. (2013):

$$\nabla \cdot F_o(\phi) = \begin{cases} Q_{NH} \frac{1}{\cos\phi} \left(1 - \frac{2\phi^2}{{\phi_{NH}}^2}\right) \exp\left(\frac{-\phi^2}{{\phi_{NH}}^2}\right), & \text{if } \phi > 0 \\ Q_{SH} \frac{1}{\cos\phi} \left(1 - \frac{2\phi^2}{{\phi_{SH}}^2}\right) \exp\left(\frac{-\phi^2}{{\phi_{SH}}^2}\right), & \text{if } \phi < 0. \end{cases} \tag{2}$$

In the all-ocean simulation, we used a symmetric setup with NH and SH ocean Q flux amplitudes $Q_{NH} = Q_{SH} = 20$ and widths $\phi_{NH} = \phi_{SH} = 16°$. For each simulation including land, Q_{NH} and ϕ_{NH} are varied (Table 1) so that the ocean heat transport (the meridional integral of the Q flux) approaches zero at the coastline (Fig. 2b). Every simulation was performed with T85 horizontal spectral resolution with 30 vertical levels and run for 20 years. Only data averaged over the last 10 years was used in the analyses to account for the model spin up. Because land and ocean differ only by their mixed layer depth, the only aspect of the land-sea contrast we account for is the capability of the ocean to store and transport energy due to its higher thermal inertia and prescribed ocean Q flux.

b. Monsoon Onset Metrics

To quantitatively analyze the influence of continental geometry on the monsoon onset timing, we calculate monsoon onset using two methods that try to capture the occurrence of the rapid intensification of summertime tropical precipitation associated with the monsoon. One method identifies onset as the pentad at which the mean precipitation (averaged over 10° to 30°) first exceeds its annual mean, similar to Zhou and Xie (2018) and to which we refer to as the ZX18 index. We also calculate onset following the method described in Walker and Bordoni (2016), to which we refer to as the WB16 index. The WB16 index is based on detecting the change point of a two-phase linear regression of the cumulative moisture flux convergence (CMFC) over a representative region (here taken as the latitudinal band between 0° and 30°, Fig. 5). Because the moisture flux convergence primarily balances net precipitation, this index detects onset as the time at which net precipitation switches from negative to positive (and withdrawal as the opposite transition).

c. Data

To draw comparison between monsoons simulated by our idealized experiments and observed monsoons, we use the Global Precipitation Climatology Project (GPCP) daily precipitation taken over 1997−2012. Fig. 4 shows the seasonal cycle of precipitation averaged in longitude over the different NH monsoons. The onset of the South Asian monsoon (SAM, Fig. 4a), the largest-scale of Earth's monsoons, appears as a rapid and dramatic rearrangement of the precipitation patterns, with the main convergence zone shifting rapidly from the near-equatorial ocean into the subtropical continent. Another striking feature is the asymmetry between a rapid onset and a much more gradual retreat. While also featuring somewhat rapid onsets, other monsoons (Fig. 4b and c) do not feature the same poleward extension of the monsoonal rains and the same degree of asymmetry between a rapid onset and a more gradual retreat. We will try to use our experiments to ascribe some of these differences to differences in land-sea distribution.

3. Seasonal Cycle

As discussed in the Introduction, in this study we regard the monsoon as excursions into subtropical latitudes of the ITCZ embedded within the ascending branch of the cross-equatorial Hadley cell. While several ITCZ metrics exist in the literature, here we identify the ITCZ as the location of the precipitation maximum and we examine its seasonal evolution to track the monsoon development. In this section, we begin by reviewing the observed seasonal cycle of the lower-level horizontal winds and streamfunction, in addition to that of precipitation. Next, we compare the calculated ITCZ with three different ITCZ predictors based on energetic arguments to explore their relationship with the development of the monsoon.

a. Temporal Structure

Here, we characterize the seasonal cycle of tropical precipitation by tracking the location of the ITCZ, generally defined as the maximum in tropical precipitation, of and other related metrics to be described below. We recognize that one single parameter does not capture the complexity of the precipitation distribution (Popp and Lutsko 2017), but for the purpose of studying the trends discussed in this section, our metric captures the most important changes.

The seasonal cycle of precipitation from each of the six simulations performed is depicted in Fig. 3 (color contours). The precipitation temporal structure in simulations with land extending into the tropics northward of 0°, 10°, and 20° all have a similar striking asymmetry, characterized by a rapid cross-equatorial jump of the ITCZ from the Southern hemisphere (SH) into the NH during NH spring and a slower retreat back to the SH in NH fall. The 10° simulation can be considered a good analog for the South Asian Monsoon: in addition to land extending polewards from low latitudes over a large longitudinal range in the NH and ocean in the SH, MLDs over the Indian Ocean north of 10-15° do not exceed 10 m in May just before monsoon onset (Walker 2017). It is striking that a simple zonally symmetric continent with equatorward boundary confined within 20 degrees of the equator produces a monsoon with a rapid onset and gradual retreat similar to what observed in the SAM region (Fig. 4a).

The 30° and 40° simulations look generally similar to the all-ocean aquaplanet results. In these simulations, the ITCZ progression is relatively smooth over the whole year, and the rapid ITCZ transition distinct to the monsoon is no longer observed. It is also noted that in every simulation with land, there is a local maximum in precipitation over the coastline during NH summer. Further analysis of the fraction of precipitation due to moisture flux convergence calculated as $(P-E)/P$, where precipitation is P and evaporation is E, shows that these coastline precipitation maxima are primarily due to local recycling of moisture, whereas the main ITCZ band is due to moisture flux convergence by the large-scale overturning circulation. For example, in the 40° simulation, the fraction of the total precipitation that is explained by the moisture flux convergence $(P-E)/P$ along the coastline does not exceed 10%, indicating the dominant role of local evaporation. In the 10° simulation, local evaporation in the main convergence zone plays a larger role at the beginning of the rainy season, with $(P-E)/P \sim 30\%$ early in the summer (May-June) compared to $(P-E)/P \sim 70\%$ during the peak of the summer. As we will show in Section 4, the corresponding circulations are also in different dynamical regimes. We recognize that these secondary precipitation maxima are artifacts of using a fully saturated surface in our model. Future work will include further steps towards realism by, for instance, limiting evaporation over land (e.g., Voigt et al. 2016).

Not only does continental geometry affect the temporal symmetry of the progression of tropical precipitation, but also its timing. Monsoon onset, according to both indices used here, tends to become increasingly delayed as the southern boundary of the land is moved further poleward. For example, onset for the 10° and 20° simulations occurs around May, while it is delayed to around June for the 30° and 40° simulations. Interestingly, the timing of monsoon retreat seems to be less strongly influenced by continental geometry. As can be seen in Table 2, the onset dates vary over a span of more than two months between the simulations, with earlier monsoon onsets occurring in simulations with more land extending into the tropics. In contrast, the retreat dates vary over the span of less than one month between the simulations, all occurring in early to late October. One of the advantages of the WB16 index is that it reveals not only the timing of monsoon onset, but also its rapidity: as seen in Fig. 5, in the simulations with southern boundary equatorward of 20°, the pick up of CMFC after monsoon onset is rapid, as the circulations intensifies rapidly and so does the moisture flux convergence in the tropical region. In contrast, the 30°, 40°, and all-ocean simulations show relatively more gradual changes in the CMFC, reflective of less rapid changes in the circulation.

Together with precipitation, Fig. 3 also shows the distribution of the lower-level MSE (magenta lines). The near-surface MSE distribution shows similar features as the precipitation distribution, in agreement with convective quasi-equilibrium (CQE) theories of monsoonal precipitation that link the ITCZ to the lower-level MSE maximum (e.g., Emanuel 1995; Privé and Plumb 2007a). The 0°, 10°, and 20° simulations show an abrupt poleward jump in the MSE maximum that coincides with the rapid ITCZ transition during NH spring. An interesting double maxima structure is also observed during the height of the monsoon during which time there is also a double ITCZ. The transition during NH fall is much more gradual. Like in the precipitation distributions, the near-surface MSE transitions in the 30°, 40°, and all-ocean experiments are relatively smoother.

To explore how these precipitation patterns reflect on circulation patterns, Fig. 6 shows the seasonal cycles of the lower-level ($\sigma = 0.887$) mass streamfunction and zonal wind. In each simulation, the ascending branch of the streamfunction closely follows the precipitation maximum, where a more asymmetric temporal structure and further poleward extent are observed in the 0°, 10°, and 20° simulations relative to those of the 30°, 40°, and all-ocean simulations. At monsoon onset in the 0°, 10°, and 20° simulations we observe a rapid intensification of the lower-level westerlies within the winter Hadley cell, compared to a relatively weaker and delayed onset of westerlies in the 30°, 40°, and all-ocean simulations. This is made more apparent in Fig. 7, where we show the lower-level zonal wind u_{low} at 15°S, the equator, and 15°N for the 10° simulation, as representative of the monsoon-like case, and the 30° simulation, more representative of an ocean-like tropical ITCZ. Note that we will focus on these two simulations in all plots hereafter. At 15°N, both simulations show a reversal of u_{low} from easterlies to westerlies during NH summer. However, the wind reversal is more rapid and the duration of the westerly flow much longer in the 10° simulation than the 30° simulation. The establishment of lower-level westerly flow primarily results because the dominant zonal momentum budget in the boundary layer is a balance between the Coriolis force and friction:

$$f\overline{v} = \kappa\overline{u}. \tag{3}$$

Westerlies must hence develop whenever northward (southward) meridional flow exists in the NH (SH). In the 10° simulation, the rapid intensification of the summer westerlies is in fact concomitant with the rapid increase in meridional winds in the circulation lower branch and rapid growth in the extent of the winter Hadley cell at monsoon onset (Fig. 6, also see Fig. 9). In contrast, the summer westerlies in the 30° simulation do not increase in magnitude as much as in the 10° simulation, and also intensify later in the season, consistent with a more slowly growing winter Hadley cell that does not extend as far into the summer hemisphere as that in the 10° simulation.

b. Connection Between the ITCZ and the Energetics

Here, we explain differences in the seasonal ITCZ progression across the different simulations in terms of energetic constraints, and associated ITCZ predictors (e.g., Kang et al. 2008; Bischoff and Schneider 2014). The first ITCZ metric is the maximum in lower-level MSE (MSE_{max}, Privé and Plumb 2007a). The other two ITCZ predictors are the energy flux equator (EFE), which is the latitude at which the total energy transport vanishes (e.g., Kang et al. 2008) and its analytical approximation (c.f., Bischoff and Schneider 2014)

$$\delta \approx -\frac{1}{a}\frac{\langle\overline{vh}\rangle_0}{\partial_y\langle\overline{vh}\rangle_0} = -\frac{1}{a}\frac{\langle\overline{vh}\rangle_0}{\overline{NEI_0}}, \tag{4}$$

where δ is the displacement of the EFE off the equator, $\langle vh \rangle$ is the vertically integrated meridional MSE transport and NEI is the net energy input into the atmospheric column (equaling the difference between the TOA radiative fluxes and surface radiative and turbulent enthalpy fluxes). The subscript 0 indicates that the quantity is calculated at the equator, and a is the radius of the Earth. We refer to δ as BS14. For the ITCZ and all three predictors, averages are taken over both of the solsticial seasons to see how changing hemispheric asymmetry in thermal inertia can affect the poleward migration of the ITCZ. Given the differences in monsoon onset and withdrawal timing across simulations, averages for both NH and SH summers are computed over 15-pentad time intervals centered around the time of maximal excursion.

Not surprisingly, continental geometry has a strong impact on the poleward extent of rainfall (Fig. 8), in addition to its influence on the timing of the monsoon transition. In the simulations with land (southern boundaries of land at 0°, 10°, 20°, 30°, and 40°), while the magnitudes of the ITCZ and predictors vary slightly, they agree well on two main general trends. First, during both NH summer and SH summer, the poleward extent of the ITCZ decreases as the southern boundary of the continent is moved further poleward and the hemispheric asymmetry in thermal inertia is decreased. Second, in each simulation, the NH summer ITCZ tends to extend further poleward than the SH summer ITCZ. This asymmetry in the poleward extent between NH summer and SH summer decreases as the continent is moved further from the equator. For example, in the 0° simulation the NH summer ITCZ extends $\sim 9°$ further poleward than the SH summer ITCZ. As the southern boundary of land is progressively moved away from the equator, for instance in the 30° simulation, the difference between the NH summer ITCZ and SH summer ITCZ reduces to $\sim 1°$, to then approach the same value in the 40° case. Notice how in the SAM region, there is a large asymmetry in the observed summertime vs. wintertime ITCZ position (Fig. 4): the JJA mean ITCZ extends to 17.7°, compared to the DJF mean ITCZ which only extends to -5.9°.

As discussed earlier, the land-sea configuration in the SAM sector is the one that more closely resembles the idealized simulations with larger hemispheric asymmetry, that is, with a continent extending to tropical latitudes. The resulting hemispheric asymmetry in NEI, therefore, results in a larger poleward excursion of the summertime ITCZ. In this respect, land-sea contrast matters to the extent it can push the ITCZ far enough off the equator, in association with Hadley circulations that become more strongly cross equatorial. We also note that in the majority of the simulations, the ITCZ predictors based on CQE theory and the energetic framework are observed further poleward than the ITCZ during solsticial seasons. This is not surprising, as these are all proxies for the poleward extent of strong winter, cross-equatorial circulations, rather than maximal precipitation. As the asymmetry between the winter and the summer cell increases, the region of strongest vertical motion, and hence precipitation, is progressively more separated from and located further equatorward of the poleward circulation edge (Faulk et al. 2017; Lobo and Bordoni 2020). One exception worth of note is the EFE during austral summer, which is found to be equatorward of the ITCZ in almost all simulations. This arises because the EFE leads the ITCZ, with the lead time increasing with the larger mixed layer depth of the ocean (Wei and Bordoni 2018) and because at the beginning of boreal summer, the EFE shifts quite rapidly onto the continent. Hence, the resulting averages give values that are equatorward of the maximal precipitation.

Fig. 8 also shows the ITCZ and the three ITCZ predictors for the all-ocean simulation. Interestingly, the poleward extents of the NH summer and SH summer ITCZs are slightly larger than what is seen in the 40°. This might be because in the all-ocean simulation, precipitation maxima with wider latitudinal ranges but lower intensities are observed during NH summer and SH summer relative to the those observed in the 40° simulations (Fig. 3), allowing slightly more poleward solsticial ITCZs.

From the results presented above, only the simulations with land extending from the north pole down to $0°$, $10°$, and $20°$ are able to reproduce the rapid cross-equatorial jump of the ITCZ and reversal of zonal winds characteristic of the monsoon. The energetic framework allows to interpret these results, at least in terms of seasonally-averaged ITCZ metrics, through the impact of the land masses on the interhemispheric asymmetry in net energy input into the atmospheric column. Next, we move to explore more closely the transitions into the summertime monsoon regime by studying the underlying dynamics.

4. Role of Dynamics

To better understand the mechanisms that drive the tropical circulation to produce seasonal cycles as observed in Section 3, we look more closely at the overturning circulation to relate its seasonal transitions to recent monsoon dynamical theories (Schneider and Bordoni 2008; Bordoni and Schneider 2008; Geen et al. 2018).

a. Theory

Schneider and Bordoni (2008) and Bordoni and Schneider (2008) showed that the rapidity of the monsoon transitions in idealized aquaplanet simulations can be explained as a switch between two dynamical regimes that differ in the amount of influence eddy momentum fluxes have on the strength of the tropical circulation. The zonally averaged steady-state zonal momentum budget in the upper branch of the circulation is approximately:

$$(f + \overline{\zeta})\overline{v} = f(1 - R_o)\overline{v} \approx \mathcal{S}, \tag{5}$$

with planetary vorticity $f = 2\Omega \sin\phi$, relative vorticity $\zeta = -\partial\overline{u}/\partial y$, local Rossby number $R_o = -\overline{\zeta}/f$, and transient eddy momentum flux divergence (EMFD) $\mathcal{S} = \partial\overline{u'v'}/\partial y + \partial\overline{u'\omega'}/\partial p$. Here we will continue to express all quantities in cartesian coordinates, even though both the model and our calculations below are in spherical coordinates. As discussed in Schneider (2006), R_o is a measure of how far (small R_o) or close (R_o approaching 1) the circulation is from the angular momentum conserving (AMC) limit. In the first case, that is $R_o \to 0$, Eq. 5 reduces to $f\overline{v} \approx \mathcal{S}$. In this regime, AM contours are vertical and the mean meridional circulation $\overline{v}$ is tied to the EMFD. When $R_o \to 1$, the meridional AM gradient following the streamlines in the upper branch of the circulation approaches zero, and Eq. (5) becomes a trivial balance, no longer providing constraints on the circulation strength. In this limit, hence, the circulation responds more directly to the thermal forcing (Held and Hou 1980; Lindzen and Hou 1988).

Bordoni and Schneider (2008) and Schneider and Bordoni (2008) demonstrated that this dynamical framework applies well to monsoon dynamics. They found that the rapid transition of the ITCZ and strengthening of the winter Hadley cell characteristic of monsoons coincides with a switch from a dynamical regime strongly influenced by eddies to a regime where the MOC is close to the AMC limit. More specifically, in their simulation, a uniform lower boundary with low thermal inertia allows the MSE maximum, and with it the poleward boundary of the tropical circulation, to move rapidly off the equator. This also allows the circulation to intensify rapidly as it transitions to being AMC. In this section, we aim to test directly how the presence or absence of land in the tropics and subtropics can affect these dynamical transitions. More specifically, we investigate how changing the hemispheric asymmetry in thermal inertia can favor or disfavor the relative influence of eddies on the strength of the MOC at different times of the seasonal cycle and impact the rapidity of the transition.

b. Results

Here we focus on the 10° and 30° simulations at two representative time periods. The two different time periods (denoted in Fig. 3) are 20 day periods centered around two pentads (June 21 and September 11, respectively), which represent different phases of the monsoon development in the 10° simulation: the first pentad captures the initial phase, where local moisture recycling still contributes significantly to continental precipitation; the second pentad, instead, coincides with the peak of the monsoon, when the precipitation is mostly due to the moisture flux convergence by the broad tropical overturning circulation.

Fig. 9 shows the total streamfunction Ψ of the mean meridional circulation (black) and the angular momentum contours (magenta) from the 10° simulation. Prior to the monsoon transition in early NH summer around June 21, a single strong cross-equatorial circulation cell is not yet established, instead, two smaller circulation cells are observed, which may be due to the two local maxima in sub-cloud MSE. Note how the AM contours are not completely aligned with the streamlines even in the ascending and upper branch, suggesting deviation from AM conservation. In the accompanying plot of precipitation and lower-level MSE, the MSE features one obvious maximum at $\sim 20°$ and a more subtle maximum at $\sim 10°$ due to the low thermal inertia over land and faster heating over the coastline during NH spring. This double-maxima MSE structure causes two counterclockwise circulation cells that have precipitation maxima located at the ascending branch of each cell, which explains the double ITCZ structure observed in Fig. 3. By September 11, a strong broad cross-equatorial winter Hadley cell is established with a weaker summer Hadley cell located north of it. In the upper branch, Ψ is now parallel to the AM contours and the circulation is in the AMC regime. This is the strong tropical summer circulation associated with the monsoon. The rapid movement of the lower-level MSE into subtropical latitudes made possible by the low heat capacity of land (Fig. 3) allows the cross-equatorial circulation to strengthen and expand rapidly. These rapid circulation changes allow for similarly rapid precipitation changes. We also note the existence of a secondary precipitation maximum, located on the summer side of the equator. This secondary precipitation maximum is a very common feature of cross-equatorial circulations in both idealized and realistic simulations (e.g., Privé and Plumb 2007a) and, as detailed in Lobo and Bordoni (2020), coincides with a region where the near-surface meridional temperature gradient changes sign. This result is consistent with the boundary layer dynamics described in Pauluis (2004), by which the flow must jump into the free troposphere in regions where the pressure gradient cannot sustain the required poleward flow.

The results from the 30° simulation (Fig. 10) show a different picture. Around June 21, the cell structure is more complicated than in the 10° simulation. A counterclockwise circulation is still observed just south of the equator and above the coastline at $\sim 30°$, but a smaller clockwise circulation exists between them. The ascending branches of the two counterclockwise cells coincide with the lower-level MSE and precipitation maxima. The upper branches of the overturning cells cross the AM contours, which are essentially vertical. Around September 11 a broad winter Hadley cell is observed; while distortion of the AM contours from the vertical is seen, the circulation seems to be less efficient at homogenizing AM than that of the 10° case at the same time. Below we will provide further analysis to assess more quantitatively how close the circulation is in the two simulations to the AMC limit. One thing to bear in mind is that compared to the 10° simulation, the MOC in the 30° simulation extends over regions of larger thermal inertia, which prevents the lower-level MSE from adjusting as rapidly as in the 10° simulation. Hence, the development of a cross-equatorial cell into the summer hemisphere that approaches AM conservation occurs more gradually. This suggests that EMFD influences the circulation strength for a longer part of the NH summer, delaying the transition into the dynamical regime where the flow approaches the AMC limit and preventing the circulation to grow rapidly in strength and extent. In this respect, monsoon-like rapid transitions cannot occur if land remains limited to higher latitudes, as the circulation responds more linearly to the seasonal insolation changes.

To further investigate the influence of eddies on the MOC, we decompose the total streamfunction Ψ (c.f. Schneider and Bordoni 2008) into a component associated with eddy momentum fluxes

$$\Psi_e(\phi, p) = -\frac{2\pi a \cos\phi}{fg} \int_0^p \mathcal{S} dp' \tag{6}$$

and a component associated with the mean momentum flux

$$\Psi_m(\phi, p) = -\frac{2\pi a \cos\phi}{fg} \int_0^p \mathcal{M} dp' \tag{7}$$

where $\mathcal{M}$ is the mean momentum flux divergence and p is the pressure. Above the boundary layer where frictional processes can be neglected, $\Psi = \Psi_e + \Psi_m$. Fig. 11 shows Ψ_e and Ψ_m (black line) over the EMFD (color) from the 10° and 30 ° simulations at June 21 and September 11. In the 10° simulation around June 21, Ψ_m starts to dominate in both hemispheres as Ψ_e starts to decrease in the subtropics (Fig. 11a). Around September 11 when the monsoonal circulation is broad and strong, Ψ_m clearly dominates globally and has strengthened since June 21 (Fig. 11b). In fact, Ψ_e is only dominant at around 30°S, expanding the extent of the circulation's descending branch in the winter hemisphere. We note that the NH maximum in Ψ_e in the tropics is associated with eddy momentum flux convergence located in the upper troposphere above the Ψ_e maximum. As discussed in previous work, this is indicative of a source of eddy activity (Held 2000), and happens where the absolute vorticity gradient changes sign, a necessary condition for barotropic instability in the cross-equatorial cell (Pedlosky 1964). In the 30° simulation around June 21, both Ψ_e and Ψ_m are much weaker than those at the same time in the 10° simulation and have equal influence on Ψ (Fig. 11c). Around September 11, Ψ_m dominates both hemispheres over Ψ_e (Fig. 11d). These results hence show how, once the winter Hadley cell becomes broad and well established, the influence of eddies on the strength of the circulation decreases as the MOC gets closer to the

AMC limit. They also demonstrate the importance of having land extend into the tropics to enable the transition into the AMC dynamical regime to occur on a rapid intraseasonal timescale.

The role that land in the low latitudes plays in the rapid dynamical regime transition of the MOC becomes more apparent if we look at the seasonal cycle of the terms in the upper-level ($\sigma = 0.195$) zonal momentum budget in Eq. (5) (Fig. 12) and the upper-level zonal wind u_{up} (Fig. 13). The zonal mean Coriolis term $f\overline{v}$ is approximately balanced by the sum of the mean flow advection $-(\overline{v}\partial\overline{u}/\partial y + \overline{\omega}\partial\overline{u}/\partial p)$ (note that in Eq. (5) the vertical advection term is neglected) and the transient eddy momentum flux convergence (EMFC) $-(\partial\overline{u'v'}/\partial y + \partial\overline{u'\omega'}/\partial p)$. In the 10° simulation, during NH summer the poleward extent of the winter Hadley cell rapidly increases starting near June 21 (marked), and gradually retreats after September 11 (marked) around late September (Fig. 6). Simultaneously, over the entire extent of the winter Hadley cell, the magnitude of the zonal mean Coriolis term $|f\overline{v}|$ increases (Fig. 12a), with large negative values in the NH $(f > 0)$ and large positive values in the SH $(f < 0)$ due to the strong southward flow $(\overline{v} < 0)$ over the entire cell. At the same time over the winter Hadley cell, the mean flow advection (Fig. 12b) strongly dominates over the transient eddy flux convergence (Fig. 12c) and approximately balances the Coriolis term. The magnitude of the mean flow advection is especially pronounced in the SH range of the winter Hadley cell. This coincides with a rapid intensification of the upper-level easterlies, which do not support westward propagating extratropical eddies (Charney 1969; Webster and Holton 1982), over the entire winter Hadley cell during the NH summer (Fig. 13a), in agreement with axisymmetric theories (c.f. Lindzen and Hou 1988). The development of the upper-level easterlies in a broad latitudinal range helps shield the winter cell from the eddy influence, which in fact remains confined only to the cell descending branch in the winter hemisphere (Fig. 12c).

In the 30° simulation, this dynamical regime transition is delayed and weaker. The expansion of the winter Hadley cell into the NH subtropics is more gradual than observed in the 10° simulation, and occurs later in the season around July (Fig. 6). The circulation not only has a smoother and delayed transition onset, but also does not extend as far polewards as the winter Hadley cell during NH summer in the 10° simulation, reaching only $\sim$20° in the 30° simulation, compared to $\sim$30° in the 10° simulation. The effects of the delay and weakening of the transition, as well as the reduced poleward extent of the winter Hadley cell, are observable in the upper-level zonal mean momentum balance, plotted in Figs 12d, e, and f. During NH summer, the intensification of the Coriolis term, which is reflective of the intensification of the cross-equatorial flow, is delayed. Simultaneously, the mean flow advection term dominates over the transient EMFC in the balance with the zonal mean Coriolis term; however its relative dominance over the transient EMFC is weaker and occurs later in the season in the 30° simulation relative to in the 10° simulation. During NH summer, the upper-level easterlies within the winter Hadley cell in the 30° simulation (Fig. 13b) are also much weaker than those in the 10° simulation (Fig. 13a), maximimizing at 21.9 m s^{-1} in the 30° simulation, in comparison to 60.2 m s^{-1} in the 10° simulation. The onset of the strengthening of the upper-level easterlies in the NH subtropics is also delayed in the 30° simulation compared to the 10° simulation, occurring only around July in the 30° simulation, compared to June in the 10° simulation. The weakening and delay of the intensification of upper-level easterlies, as well as their reduced meridional extent, delay the timing and limit the latitudinal range over which the easterlies can effectively shield the tropical circulation from the influence of the extratropical eddies. This emphasizes that, while the tropical circulation eventually approaches the AMC regime in the 30° simulation, it does so later in the season. Overall, the seasonal cycles of the terms in the upper-level zonal momentum balance and u_{up} demonstrate that having land in the tropics can influence the monsoon onset mainly through enabling the circulation to switch rapidly from the regime where the MOC strength is tied to the extratropical baroclinic eddies to the regime where the upper-level easterlies strengthen and shield the MOC from the influence of the eddies and allow the circulation to reach the AMC limit. Tropical land is hence necessary for the development of strong monsoons with a rapid development in so far as it provides a lower boundary with heat capacity that is low enough to allow for rapid near-surface MSE adjustments that initiate the dynamical feedbacks described above.

We also note that having land extend into the NH tropics and exaggerating the hemispheric asymmetry in thermal inertia also affects the magnitudes of seasonal mean eddy momentum fluxes and Ψ, not just the intraseasonal transitions. In the seasonal cycles of transient EMFC in both the 10° and 30° simulations in Figs.12c and f, stronger eddy momentum fluxes are observed in the midlatitudes during winter over land (NH winter), compared to winter over the ocean (SH winter). This is due to stronger meridional temperature gradients and therefore increased baroclinicity owing to the lower heat capacity of land surface compared to the ocean surface.

In summary, the main differences observed between the simulations with land extending north of 10° versus 30° is that in the 10° case the influence of eddy momentum fluxes on the circulation begins to decrease earlier in the season, allowing the broadening and strengthening winter Hadley cell to reach the AMC limit earlier and more rapidly. This suggests that in order to have the rapid ITCZ transitions observed in monsoons, regions of low thermal inertia are needed closer to the equator to help the MOC transition from a dynamical regime where eddies strongly influence the circulation into the AMC regime that enables the Hadley cell to directly respond to thermal forcing and grow and strengthen rapidly.

5. Discussion

The dynamics of rapid monsoon transitions such as the ones discussed in the previous section have recently been reinterpreted by Geen et al. (2018) in terms of the upper-level vorticity budget. In this section, we hence want to relate our results to those of Geen et al. (2018) by analyzing the seasonal cycle of the different terms in the vorticity budget, given by:

$$\frac{\partial \zeta}{\partial t} = -\mathbf{u} \cdot \nabla(\zeta + f) - \omega \frac{\partial \zeta}{\partial p} - (\zeta + f)\nabla \cdot \mathbf{u} + \mathbf{k} \cdot \left(\frac{\partial \mathbf{u}}{\partial p} \times \nabla \omega \right). \tag{8}$$

The vorticity tendency on the LHS is balanced by the of the terms on the RHS, which represent from left to right the horizontal advection of vorticity, the vertical advection of vorticity, vortex stretching, and vortex tilting. In the upper troposphere where ω is small, and hence the terms with ω are small compared to the horizontal advection and vortex stretching terms, the zonally averaged vorticity budget in Eq. (8) simplifies to:

$$\frac{\partial \overline{\zeta}}{\partial t} = -\overline{v} \frac{\partial (\overline{\zeta} + f)}{\partial y} - (\overline{\zeta} + f) \frac{\partial \overline{v}}{\partial y}. \tag{9}$$

The horizontal advection and vortex stretching terms on the right hand side of Eq. (9) throughout the season therefore can be thought of as tendencies of the upper-level absolute vorticity via changes in $\overline{\zeta}$ (Geen et al. 2018). It is important to keep in mind that in the zonal mean the upper-level absolute vorticity f + $\overline{\zeta}$ is proportional to the meridional gradient of M, hence a circulation with R_o approaching 1 implies vanishing absolute vorticity in the circulation upper branch (Schneider 2006; Geen et al. 2018).

Geen et al. (2018) proposed that, at the onset of NH summer as the ITCZ crosses the equator, simultaneously the horizontal advection tendency becomes positive and the vortex stretching tendency becomes negative in the summer hemisphere. The combined effect of these two tendencies results in a latitudinally broad region of reduced magnitude of absolute vorticity that implies AM conservation within the tropical circulation and assists the circulation to decouple from the eddy momentum fluxes and become more thermally direct. By breaking down these two tendencies into their dominant terms, Geen et al. (2018) were able to show that the positive horizontal advection tendency is driven by the southward mean flow in upper branch of the winter Hadley cell in NH summer, which increases absolute vorticity in the summer hemisphere and decreases absolute vorticity in the winter hemisphere by advecting higher absolute vorticity air downgradient. The divergent flow in the ascending branch of the Hadley cell instead contributes a negative vortex stretching tendency.

The seasonal evolution of the upper-level horizontal advection and vortex stretching tendencies calculated from our 10° simulation contain similarities to those described in Geen et al. (2018). Fig. 14 displays the seasonal cycles of the upper-level horizontal advection and vortex stretching tendencies at $\sigma = 0.195$ (Fig. 14a, d), as well as the decomposition of each term into its dominant components (Fig. 14b, c, e, f). Focusing on the transition into NH summer, first we note that from the time the ITCZ crosses the equator before NH summer in May till the end of NH summer in September, from near the equator in the SH up to the winter Hadley cell poleward edge near 25°N is a region of reduced magnitude of absolute vorticity, as the circulation becomes more angular momentum conserving (Fig. 14f). This reduction in the absolute vorticity results from the combined effect of positive horizontal advection of vorticity (Fig. 14a) and negative vortex stretching (Fig. 14d), whose sum is shown in Fig. 16a. In Fig. 14a, over most of the meridional range of the winter Hadley cell from -30° up to the coastline at 10°, the horizontal advection term is positive. This corresponds to the southward mean flow and positive meridional gradient of absolute vorticity in this region, and results in a decrease in the magnitude of the negative absolute vorticity in the SH. At the same time, the vortex stretching tendency is negative over the bulk of the NH latitudinal range of the winter Hadley cell from the equator up to $\sim 30°$ due to the divergent flow in the circulation's ascending branch and the positive magnitude of the absolute vorticity in this region. The combined effect (Fig. 16a) is the observed reduction in magnitude and meridional gradient of absolute vorticity across the winter Hadley cell from May through September (Fig. 14f). We do note that during NH summer there is a region of negative horizontal advection tendency around the coastline at 10°. This results from a negative meridional gradient in vorticity over the same latitude observed (Fig. 14b), which is indicative of barotropic instability in the cell, as discussed in the previous section. However, since the positive horizontal advection mainly works to reduce the magnitude of negative absolute vorticity in the SH, this patch of negative horizontal advection at the coastline does not appear to affect the main mechanism of the horizontal advection and the overall reduced magnitude in absolute vorticity associated with a more AM conserving MOC.

Geen et al. (2018) also suggest that monsoon regime transitions coincide with peaks in the horizontal advection and vortex stretching tendencies. As the ascending branch of the Hadley circulation and peak in divergent flow move polewards during NH summer, they move from a region with near zero absolute vorticity near the equator to a region of non-negligible absolute vorticity, resulting in a rapid increase in the magnitude of the vortex stretching and a negative peak in vortex stretching. The link between the peaks in the tendencies and the dynamical regime transition is observable in our 10° simulation. Peaks in the horizontal advection and vortex stretching are in fact observed immediately following June 21, after which the extratropical eddies' influence on the MOC is weakened and the MOC transitions into a thermally driven circulation approaching the AMC limit. While the peaks in horizontal advection and vortex stretching in our 10° simulation lag the cross-equatorial jump of the ITCZ more than in the full aquaplanet simulation with 2m MLD in Geen et al. (2018), they do appear to coincide with the rapid dynamical regime transition that allows the overturing cell to grow rapidly in strength and poleward extent.

Fig. 15 contains the same results as in Fig. 14 but from the 30° simulation. The changes in horizontal advection and vortex stretching tendencies are relatively smooth and delayed compared to those from the 10° simulation. During NH summer, the positive horizontal advection (Fig. 15a) over the winter Hadley cell has a greatly reduced magnitude compared to the horizontal advection tendency over the same latitudinal range and period in the 10° simulation (Fig. 14a). This results from a much weaker MOC (comparing Fig. 14c to Fig. 15c). The region of negative vortex stretching during NH summer also extends less polewards and is less strongly negative in the 30° simulation (Fig. 15d) than that in the 10° simulation (Fig. 14d). These are results of a winter Hadley cell in the 30° simulation that does not reach as far poleward and has weaker strength, resulting in weaker horizontal divergence (Fig. 15e). Consequently, in the 30° simulation during NH summer the combined effect of the horizontal advection and vortex stretching terms (sum shown in Fig. 16b) does not reduce the absolute vorticity in the NH subtropics (Fig. 15f) as effectively as in the 10° simulation (Fig. 14f), confirming the slower transition to the AMC limit in this case. Additionally, at the start of NH summer there are no significant peaks or rapid changes in the horizontal advection and vortex stretching tendencies as observed in the 10° simulation, reflecting the more slowly evolving dynamics in the simulation with land confined to higher latitudes. This is also apparent in the very smooth evolution of the zero contour of the absolute vorticity (Fig. 14f). From the perspective of the vorticity budget, the results in Figs. 14 and 15 suggest that having land in the tropics enables the dynamical monsoon regime transition to occur on a rapid intraseasonal timescale by rapidly strengthening the divergent flow of the Hadley circulation as its ascending branch moves polewards to regions of non-negligible absolute vorticity, to quickly increase the magnitude of the vortex stretching term, and of the horizontal vorticity advection, which efficiently reduce the magnitude of the absolute vorticity and decouples the circulation from the eddy momentum fluxes.

The complementary interpretations of the dynamical monsoon regime transition are tied together by the migration of the ascending branch of the Hadley circulation. Our analyses of both the direct effect of the eddy momentum fluxes on the streamfunction (Fig. 11, 12) and the seasonal evolution of absolute vorticity (Fig. 14, 15) emphasize the importance of a significant off-equatorial migration of the ITCZ or ascending branch of the tropical MOC to initiate the rapid dynamical regime switch and monsoon onset. A more poleward migration of the ascending branch widens the winter cell's poleward extent in both hemispheres and extends the region of prevalent upper-level easterlies within the tropical circulation into a broad latitudinal band in both the summer and winter hemisphere. This helps diminish the influence of the strength of the extratropical eddies originating in the winter hemisphere on the tropical circulation by shielding the circulation and weakening the EMFD at the cell center, and therefore enables the circulation to approach the AMC limit and become more thermally driven and rapidly strengthen. A more poleward migration of the ascending branch also brings the region of strongest upper-level horizontal divergence to a region of higher absolute vorticity in the NH and strongest horizontal advection to a region of large negative magnitude of absolute vorticity in the SH, since the positive meridional gradient of absolute vorticity in the NH increases with latitude. This in turn increases the vortex stretching and horizontal advection tendencies and results in a more efficient reduction of absolute vorticity across the entire winter Hadley cell and therefore a more AMC circulation. Regardless through which interpretation, once the circulation approaches the AMC limit and becomes more thermally driven, the cell can grow rapidly in strength and extent through two dynamical feedbacks — 1) by advecting lower MSE air in its lower branch from the winter to the summer hemisphere, enabling the circulation to push the near-surface MSE maximum increasingly polewards and strengthen the temperature gradient, which by AMC requires a strengthening of the flow (Fig. 9) and 2) by also strengthening the upper-level easterlies in the winter hemisphere, effectively shielding the winter cell from the influence of the extratropical eddies and allowing it to more closely approach the AMC limit and further strengthen the upper-level easterlies (Fig. 12, 13) (Schneider and Bordoni 2008).

It is through this key ingredient — a significant off-equatorial migration of the ascending branch of the Hadley circulation — that continental geometry appears to play an important role for the monsoon. By having more land or regions of low thermal inertia in the tropics, the distribution of the near-surface MSE can evolve rapidly, and the non-linear mechanisms described above help push its maximum far enough away from the equator into the subtropics for the circulation to grow rapidly in strength and extent. Only when these nonlinear mechanisms can operate on intraseasonal timescales, can a rapid monsoon onset similar to what seen in the Asian monsoon region be seen in our simulations.

We would like to conclude this section with a brief remark on the temporal asymmetry between a rapid onset and a more gradual retreat that appears particularly evident in the simulations with continents extending to tropical latitudes. Such an asymmetry was already observed to occur in aquaplanet simulations reported by Geen et al. (2019), who attributed it to changes in SSTs induced by the wind-induced surface heat exchange (WISHE) feedback (Emanuel 1987; Neelin et al. 1987). More specifically, they argue that WISHE slows the monsoon withdrawal through weak low-level horizontal winds below the ITCZ, which keep the latent heat flux from the surface low and the SSTs warm below the ITCZ as it retreats to the winter hemisphere. Evidence of a slight temporal asymmetry between onset and withdrawal is also seen in the all-ocean aquaplanet simulation presented here. It is however clear that a large hemispheric asymmetry in thermal inertia of the lower boundary gives rise to a more pronounced asymmetry in the monsoon temporal evolution: in the presence of a continent at tropical latitudes, the lower-level MSE can adjust rapidly as the circulation transitions into the monsoon regime. As the circulation retreats from the summer hemisphere and its ascending branch moves over the ocean, its large heat capacity instead prevents rapid MSE changes, hence slowing down the withdrawal phase. We believe that the hemispheric asymmetry in the lower boundary thermal inertia might be a more relevant mechanism than the WISHE feedback for the temporal asymmetry of observed monsoons, such as the Asian monsoon. More targeted simulations, in which for instance the WISHE feedback is disabled, will shed further light into these open questions.

6. Conclusion

Altogether, this study aims to understand how changing continental geometry can affect the spatial and temporal structure of the monsoonal precipitation. Five simulations are analyzed in an idealized aquaplanet GCM, where hemispheric asymmetry in thermal inertia is varied by using different continental configurations with zonally-symmetric land extending polewards from southern boundaries at 0°, 10°, 20°, 30°, and 40° and also an all-ocean case. From studying the seasonal cycles of precipitation, near-surface MSE, mass streamfunction, and horizontal winds, we find that only the 0°, 10°, and 20° simulations with land extending into the lower latitudes have circulations with the temporal asymmetry in the rapid onset and gradual retreat characteristic of observed monsoons. By breaking down the streamfunction into eddy and mean components and analyzing the seasonal cycle of the upper-level zonal momentum budget, our simulations suggest that different continental geometry can affect the spatial and temporal structure of the circulation and precipitation by affecting the circulation's ability to transition rapidly from a regime where the tropical circulation strength is controlled by eddy momentum fluxes to a regime where the strength is more directly controlled by energetic constraints. We find that having regions of low thermal inertia in the tropics enables this transition to occur on an intraseasonal scale; in contrast without land in the low latitudes, the circulation transitions are smoother and less similar to those observed in the real South Asian Monsoon. This is because having land in the tropics allows the near-surface MSE maximum, and with it the ascending branch of the Hadley circulation, to adjust rapidly, allowing internal dynamical feedbacks to operate and to rectify the response to the smooth insolation forcing into a rapid onset.

These insights from our study help us interpret differences in various observed monsoons. The idealized continental configuration used in this study is most analogous to the SAM monsoon region (Fig. 4a), simulating well the rapid onset and gradual retreat of the monsoon, along with solsticial ITCZs extending into the subtropics. We can also gain useful insight into the factors responsible for the monsoonal precipitation onset and spatial distribution by contrasting our idealized zonally symmetric simulations with other monsoon regions. For example, while the NAM (Fig.4b) exhibits somewhat rapid monsoon onset, its summertime tropical circulation does not migrate as far poleward as that in the SAM region. While the continent in this region does extend into the tropics, it is very longitudinally confined, resulting in much less landmass within the tropics than in the SAM region. In agreement with our study's conclusion, this might prevent the development of a large-scale monsoon with an ITCZ capable of migrating significantly off the equator. Our results might also explain why the NAM lacks a well-defined cross-equatorial flow and overturning circulation, and why the QE relationship between maximal precipitation and maximal lower-level MSE does not hold in this monsoon region (Nie et al. 2010). The NAF monsoon (Fig. 4c) merits different considerations: while the NAF region does feature a longitudinally extended continent centered around the equator, its continental precipitation zone does not extend as far poleward as our simulations would suggest. As discussed in Chou and Neelin (2003), this is due to high surface albedo over northern Africa, which prevents convection to occur there by reducing the net energy input into the atmospheric column. Contrast between land and ocean due to factors other than surface thermal inertia, such as land hydrology and albedo, clearly plays an important role in determining important features of the observed monsoons and warrants further investigation.

That said, that experiments with such idealized physics and configuration can replicate important features of the observed large-scale monsoons suggests the robustness of the underlying dynamics. It is however important to further highlight the limitations in our study. First, in our simulations even land surfaces are completely saturated. In fact, at the beginning of the warm season, our simulations feature continental precipitation that is primarily driven by local evaporation, rather than moisture flux convergence. This is of course an artifact of our choice of a saturated continent and would be prevented to occur if a more realistic land surface hydrology scheme were used. Other limitations include the absence of important radiative feebacks, such as those associated with water vapor and cloud feedbacks, and, as discussed earlier, the lack of albedo contrast between land and ocean, and any zonal asymmetry. Additionally, we prescribe a zonally symmetric OHT, that neglects possible seasonality in the amplitude and direction of OHT in response to changing surface wind (Kang et al. 2018; Lutsko et al. 2019). Future work will be aimed at progressively including these effects, bridging the gap between our idealized simulations and those with comprehensive Earth System Models and observations.

Acknowledgments. This work was supported by the National Science Foundation (AGS-1462544) and the Caltech's Terrestrial Hazards Observation and Reporting (THOR) Center.

References

Adam, O., T. Bischoff, and . T. Schneider, 2016: Seasonal and interannual variations of the energy flux equator and ITCZ. Part II: Zonally varying shifts of the ITCZ. *J. Climate*, **29**, 7281–7293.

Biasutti, M., and Coauthors, 2018: Global energetics and local physics as drivers of past, present and future monsoons. *Nature Geoscience*, **11**, 392–400.

Bischoff, T., and T. Schneider, 2014: Energetic constraints of the position of the intertropical convergence zone. *J. Climate*, **27**, 4937–4951.

Boos, W. R., and R. L. Korty, 2016: Regional energy budget control of the Intertropical Convergence Zone and application to mid-Holocene rainfall. *Nature Geoscience*, **9**, 892–897.

Bordoni, S., and T. Schneider, 2008: Monsoons as eddy-mediated regime transitions of the tropical overturning circulation. *Nature Geoscience*, **1**, 515–519.

Charney, J., 1969: A further note on large-scale motions in the tropics. *J. Atmos. Sci.*, **26**, 182–185.

Chou, C., and J. D. Neelin, 2003: Tropical drought regions in global warming and El Niño teleconnections. *Geophys. Res. Lett.*, **30 (24)**.

Chou, C., J. D. Neelin, and H. Su, 2001: Ocean-atmosphere-land feedbacks in an idealized monsoon. *Quart. J. Roy. Meteor. Soc.*, **127**, 1869–1891.

Collins, M., and Coauthors, 2018: Challenges and opportunities for improved understanding of regional climate dynamics. *Nature Clim. Change*, **26**, 182–185.

Dirmeyer, P. A., 1998: Land-sea geometry and its effect on monsoon circulations. *J. Geophys. Res.*, **103**, 11 555–11 572.

Emanuel, K. A., 1987: An air-sea interaction model of intraseasonal oscillations in the Tropics. *J. Atmos. Sci.*, **44**, 2324–2340.

Emanuel, K. A., 1995: On thermally direct circulations in moist atmospheres. *J. Atmos. Sci.*, **52**, 1529–1534.

Faulk, S., J. Mitchell, and S. Bordoni, 2017: Effects of rotation rate and seasonal forcing on the ITCZ extent in planetary atmospheres. *J. Atmos. Sci.*, **74**, 665–678.

Frierson, D. M. W., 2007: The dynamics of idealized convection schemes and their effect on the zonally averaged tropical circulation. *J. Atmos. Sci.*, **64**, 1959–1976.

Frierson, D. M. W., I. M. Held, and P. Zurita-Gotor, 2006: A gray-radiation aquaplanet moist GCM. Part I: Static stability and eddy scales. *J. Atmos. Sci.*, **63**, 2548–2566.

Geen, R., F. Lambert, and G. Vallis, 2018: Regime change behavior during Asian monsoon onset. *J. Climate*, **31**, 3327–3348.

Geen, R., F. Lambert, and G. Vallis, 2019: Processes and timescales in onset and withdrawal of "aquaplanet monsoons". *J. Climate*, **32**, 2357–2373.

Held, I. M., 2000: The general circulation of the atmosphere. *Program in Geophysical Fluid Dynamics*, Woods Hole Oceanography Institution, Woods Hole MA.

Held, I. M., and A. Y. Hou, 1980: Nonlinear axially symmetric circulations in a nearly inviscid atmosphere. *J. Atmos. Sci.*, **37**, 515–533.

Hill, S. A., 2019: Theories for past and future monsoon rainfall changes. *Curr. Climate Change Reports*, **5**, 160–171.

Jeevanjee, N., P. Hassanzadeh, S. Hill, and A. Sheshadri, 2017: A perspective on climate model hierarchies. *J. Adv. Model. Earth Syst.*, **9**, 1760–1771.

Kang, S. M., D. M. Frierson, and M. Zhao, 2008: The response of the ITCZ to extratropical thermal forcing: Idealized slab-ocean experiments with a GCM. *J. Climate*, **21**, 3521–3532.

Kang, S. M., Y. Shin, and S.-P. Xie, 2018: Extratropical forcing and tropical rainfall distribution: Energetics framework and ocean Ekman advection. *NPJ Climate and Atmos. Sci.*, **1**, 1–10.

Laraia, A., 2015: Observations and modeling of tropical planetary atmospheres. Ph.D. thesis, California Institute of Technology, 37–76 pp.

Lindzen, S. R., and A. Y. Hou, 1988: Hadley circulations for zonally averaged heating centered off the equator. *J. Atmos. Sci.*, **45**, 2416–2427.

Lobo, A. H., and S. Bordoni, 2020: Atmospheric dynamics of high obliquity planets. *Icarus*, **340 (115391)**.

Lutsko, N. J., J. Marshall, and B. Green, 2019: Modulation of monsoon circulations by cross-equatorial ocean heat transport. *J. Climate*, **32**, 3471–3485.

Merlis, T., T. Schneider, S. Bordoni, and I. Eisenman, 2013: Hadley circulation response to orbital precession. Part II: Subtropical continent. *J. Climate*, **26**, 754–771.

Neelin, J. D., I. M. Held, and K. H. Cook, 1987: Evaporation-wind feedback and low-frequency variability in the tropical atmosphere. *J. Atmos. Sci.*, **44**, 2341–2348.

Nie, J., W. R. Boos, and Z. Kuang, 2010: Observational evaluation of a convective quasi-equilibrium view of monsoons. *J. Climate*, **23**, 4416–4428.

O'Gorman, P. A., and T. Schneider, 2008: The hydrological cycle over a wide range of climates simulated with an idealized GCM. *J. Climate*, **21**, 3185–3832.

Pauluis, O., 2004: Boundary layer dynamics and cross-equatorial Hadley circulation. *J. Atmos. Sci.*, **61**, 1161–1173.

Pedlosky, J., 1964: The stability of currents in the atmosphere and the ocean: Part I. *J. Atmos. Sci.*, **21**, 201–219.

Plumb, R. A., and A. Y. Hou, 1992: The response of a zonally symmetric atmosphere to subtropical thermal forcing: Threshold behavior. *J. Atmos. Sci.*, **49**, 1790–1799.

Popp, M., and N. J. Lutsko, 2017: Quantifying the zonal-mean structure of tropical precipitation. *Geophys. Res. Lett.*, **44**, 9470–9478.

Privé, N. C., and R. A. Plumb, 2007a: Monsoon dynamics with interactive forcing. Part I: Axisymmetric studies. *J. Atmos. Sci.*, **64**, 1417–1430.

Schneider, T., 2006: The general circulation of the atmosphere. *Annu. Rev. Earth Planet. Sci.*, **34**, 655–688.

Schneider, T., T. Bischoff, and G. H. Haug, 2014: Migrations and dynamics of the intertropical convergence zone. *Nature*, **513**, 45–53.

Schneider, T., and S. Bordoni, 2008: Eddy-mediated regime transitions in the seasonal cycle of a Hadley circulation and implications for monsoon dynamics. *J. Atmos. Sci.*, **65**, 915–934.

Voigt, A., and Coauthors, 2016: The tropical rain belts with an annual cycle and a continent model intercomparison project: TRACMIP. *J. Adv. Model. Earth Syst.*, **8**, 1868–1891.

Walker, C., and T. Schneider, 2006: Eddy influences on Hadley circulations: Simulations with an idealized GCM. *J. Atmos. Sci.*, **63**, 3333–3350.

Walker, J., and S. Bordoni, 2016: Onset and withdrawal of the large-scale South Asian monsoon: A dynamical definition using change point detection. *Geophys. Res. Lett.*, **43**, 11 815–11 822.

Walker, J. M., 2017: Seasonal and interannual variability in South Asian monsoon dynamics. Ph.D. thesis, California Institute of Technology, 37–76 pp.

Webster, P., and J. Holton, 1982: Cross-equatorial response to middle-latitude forcing in a zonally varying basic state. *J. Atmos. Sci.*, **39**, 722–733.

Wei, H.-H., and S. Bordoni, 2018: Energetic constraints on the itcz position in idealized simulations with a seasonal cycle. *Journal of Advances in Modeling Earth Systems*, **10 (7)**, 1708–1725.

Xie, S., and N. Saiki, 1999: Abrupt onset and slow seasonal evolution of summer monsoon in an idealized GCM simulation. *J. Meteor. Soc. Japan.*, **77**, 949–968.

Zhou, W., and S.-P. Xie, 2018: A hierarchy of idealized monsoons in an intermediate GCM. *J. Climate*, **31**, 9021–9036.

LIST OF TABLES

TABLE 1. Q flux amplitudes and widths used for each simulation.

Q flux Parameters				
Simulation	Q_{NH}	ϕ_{NH}	Q_{SH}	ϕ_{SH}
0°	0	5°	20	16°
10°	4	5°	20	16°
20°	4	7°	20	16°
30°	4	12°	20	16°
40°	4	12°	20	16°
Ocean	20	16°	20	16°

TABLE 2. Dates of monsoon onset and retreat, as calculated in Walker and Bordoni (2016)

.

Simulation	Onset	Retreat
0°	May 1	October 11
10°	May 6	October 16
20°	May 26	October 16
30°	June 11	October 16
40°	June 11	October 21
Ocean	July 16	October 21

LIST OF FIGURES

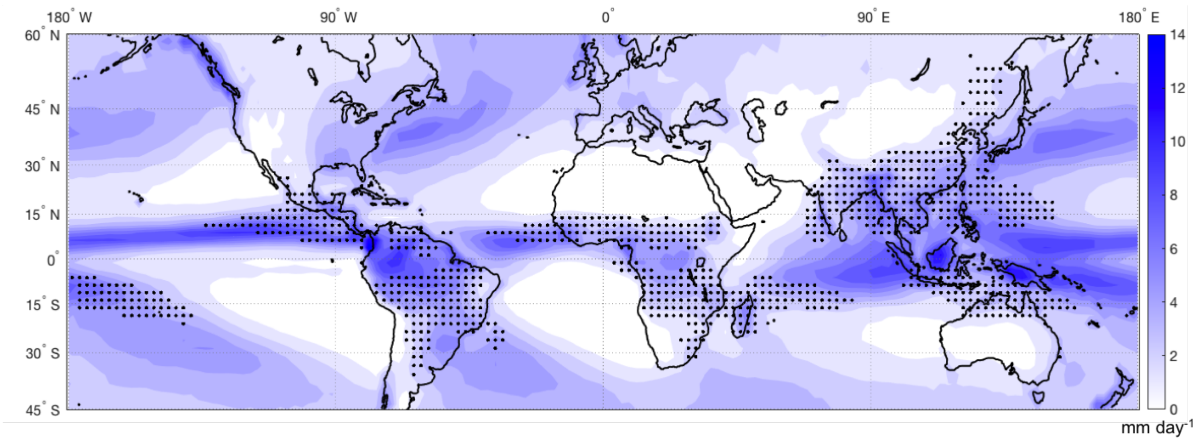

FIG. 1. Annual mean precipitation calculated from Global Precipitation Climatology Project monthly long-term mean precipitation from 1981−2010 (color). Various monsoon systems around the world (stipple) where, using only regions with local mean summer (May-September) precipitation exceeding local mean winter (November-March) precipitation by at least 2.5 mm per day, the local summer precipitation exceeds 55% of annual total.

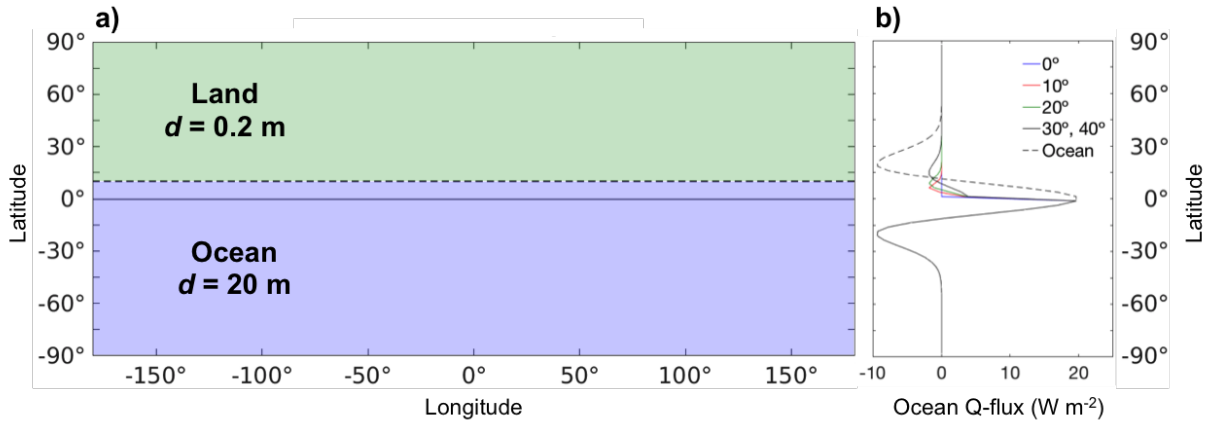

FIG. 2. Model setup: (a) schematic of continental configuration for the 10° simulation, where land has a mixed layer depth of 0.2 m and (b) the ocean Q flux distributions for each simulation.

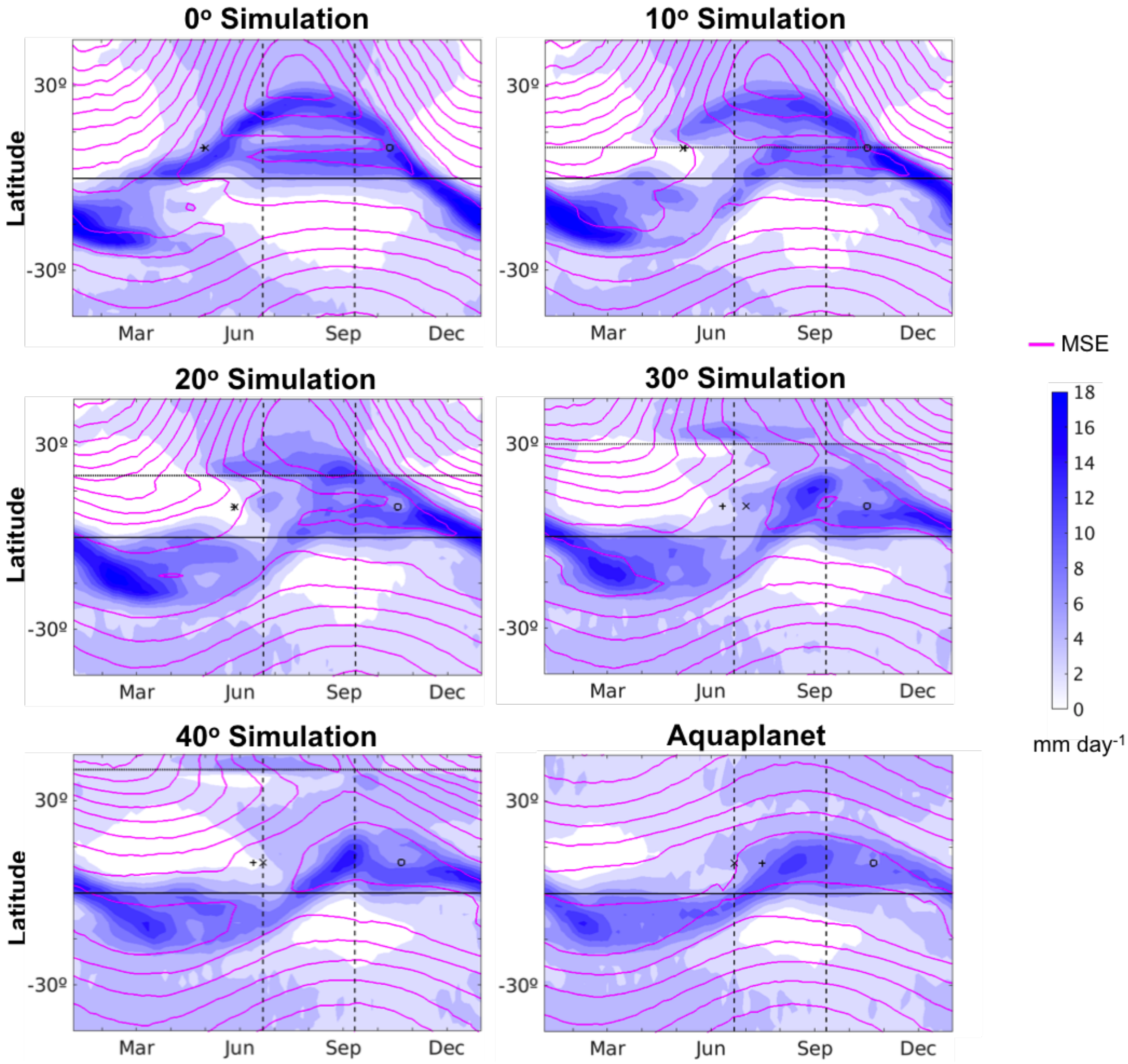

FIG. 3. Seasonal cycle of simulations with southern boundaries of land at 0°, 10°, 20°, 30°, and 40° and the all ocean aquaplanet case. Color contours indicate precipitation (contour interval 2 mm day^{-1}). Magenta contours indicate near-surface MSE taken at $\sigma = 0.887$ (contour interval 8×10^3 J kg^{-1}). The equator is marked in a solid horizontal black line and the southern boundary of land from each simulation is shown in a dotted horizontal black line. The dashed vertical lines mark June 21 and September 11, used in the analysis for Figures 9, 10, and 11. The black x's indicate monsoon onset as calculated in Zhou and Xie (2018), while the black plus signs indicate monsoon onset as calculated in Walker and Bordoni (2016).

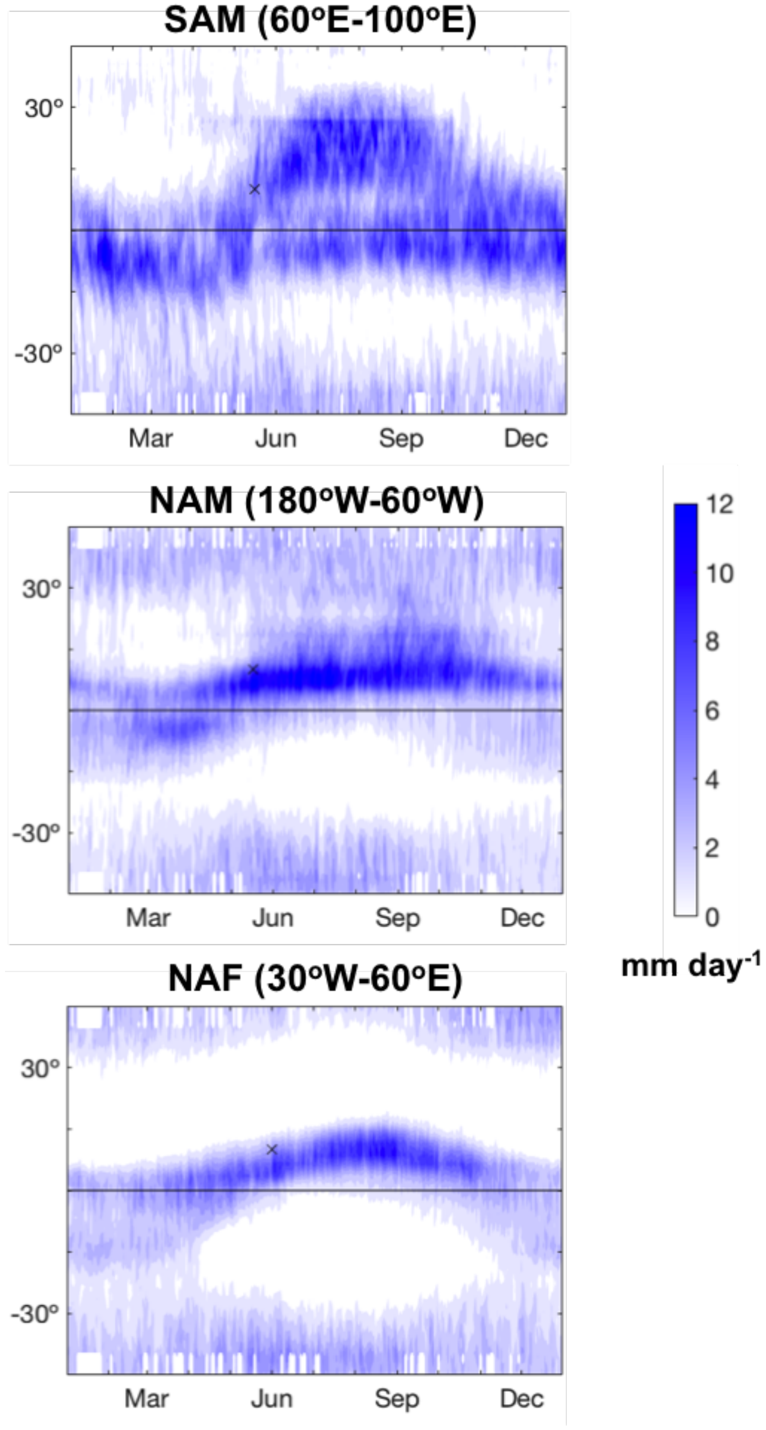

FIG. 4. GPCP daily precipitation seasonal cycle, with climatological mean taken over 1997−2012 and zonal mean taken over from top to bottom: a) the South Asian Monsoon (60$^{\circ}E - 100^{\circ}$E), b) the North American Monsoon (180$^{\circ}W - 60^{\circ}$W), and c) North African Monsoon (30$^{\circ}W - 60^{\circ}$E). Precipitation contour interval is 1 mm day^{-1}). The black cross indicates the time when the precipitation averaged from 10° to 30°N exceeds its annual mean, as in Fig. 3.

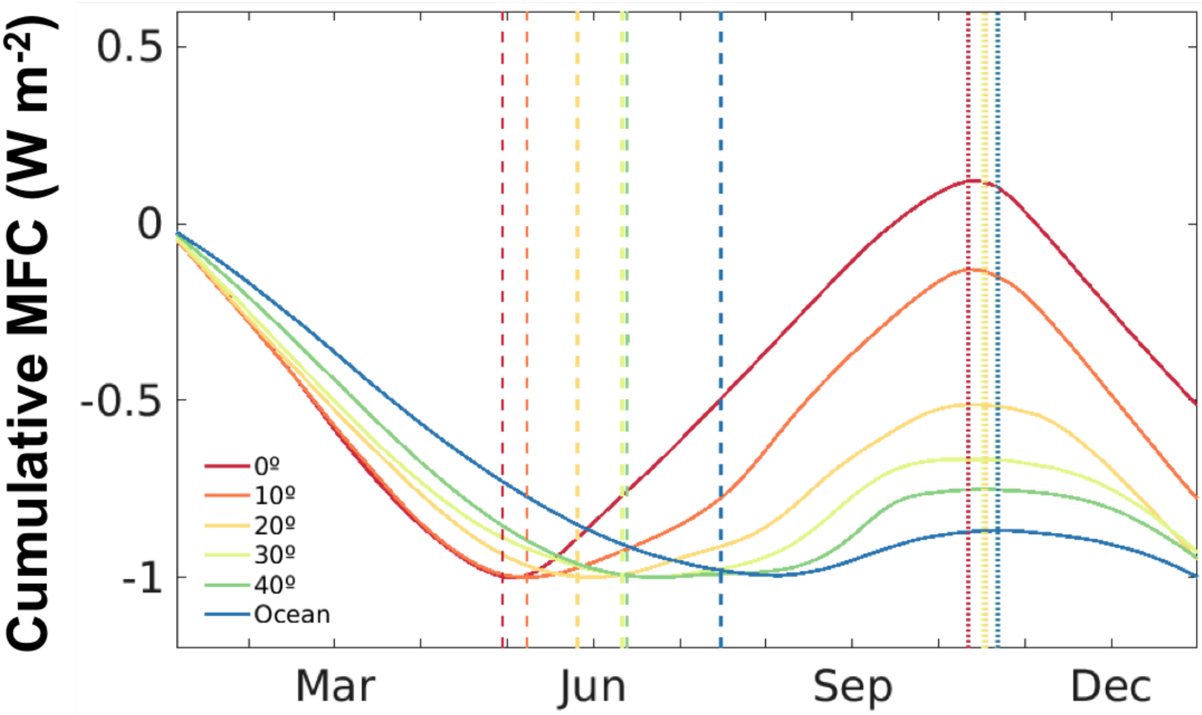

898 FIG. 5. Cumulative moisture flux convergence normalized by the minimum for each simulation from which
899 the monsoon onset and retreat indices are calculated as in Walker and Bordoni (2016). Resulting monsoon onset
900 (dashed) and retreat (dotted) indices are listed in Table 2.

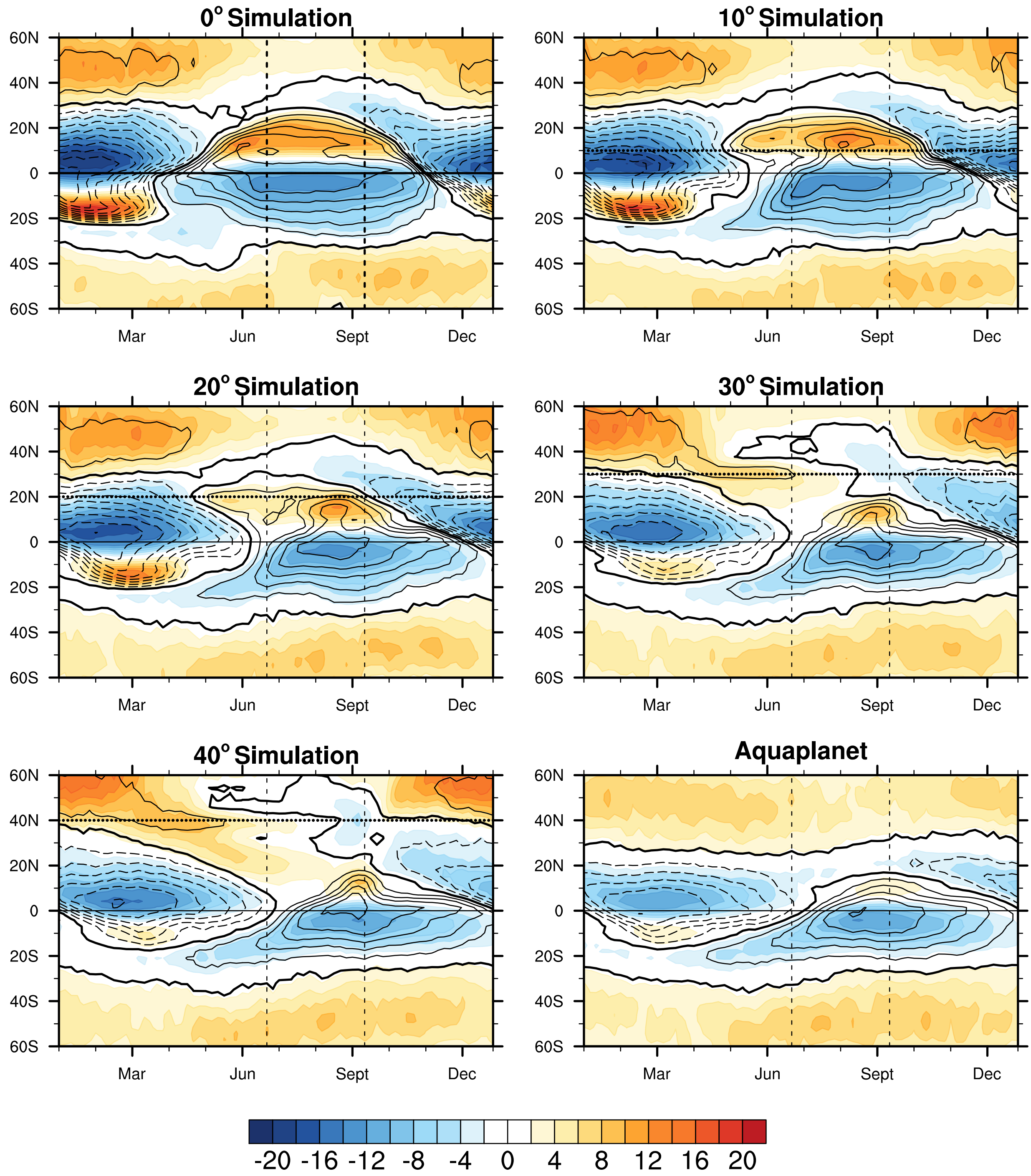

FIG. 6. Seasonal cycle of the lower-level mass streamfunction and zonal wind from simulations with southern boundaries of land at 0°, 10°, 20°, 30°, and 40° and the all ocean aquaplanet case. Color contours indicate lower-level ($\sigma = 0.887$) zonal wind (contour interval 2 m s^{-1}). Black contours mark the lower-level mass streamfunction Ψ_{low} (counterclockwise in solid, clockwise in dashed with contour interval 40×10^9 kg s^{-1}, zero contour in bold). The equator, southern boundary of the continent, and June 21 and September 11 are marked as in Fig. 3.

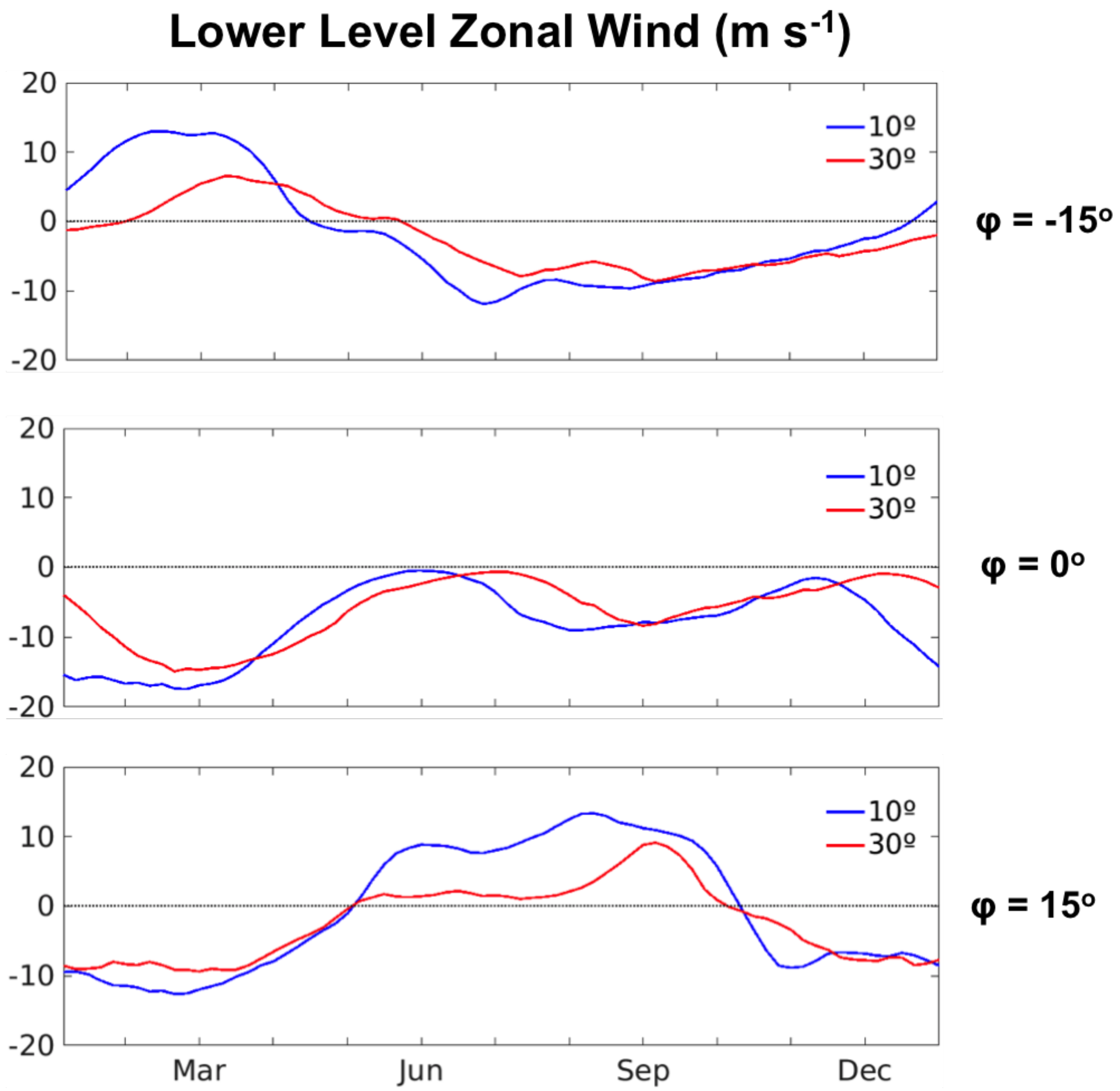

FIG. 7. Lower-level ($\sigma = 0.887$) zonal wind u_{low} for the simulations with land extending poleward from southern boundaries at 10° (blue) and 30° (red). The winds are calculated at 15°S (top), at the equator (middle), and at 15°N (bottom).

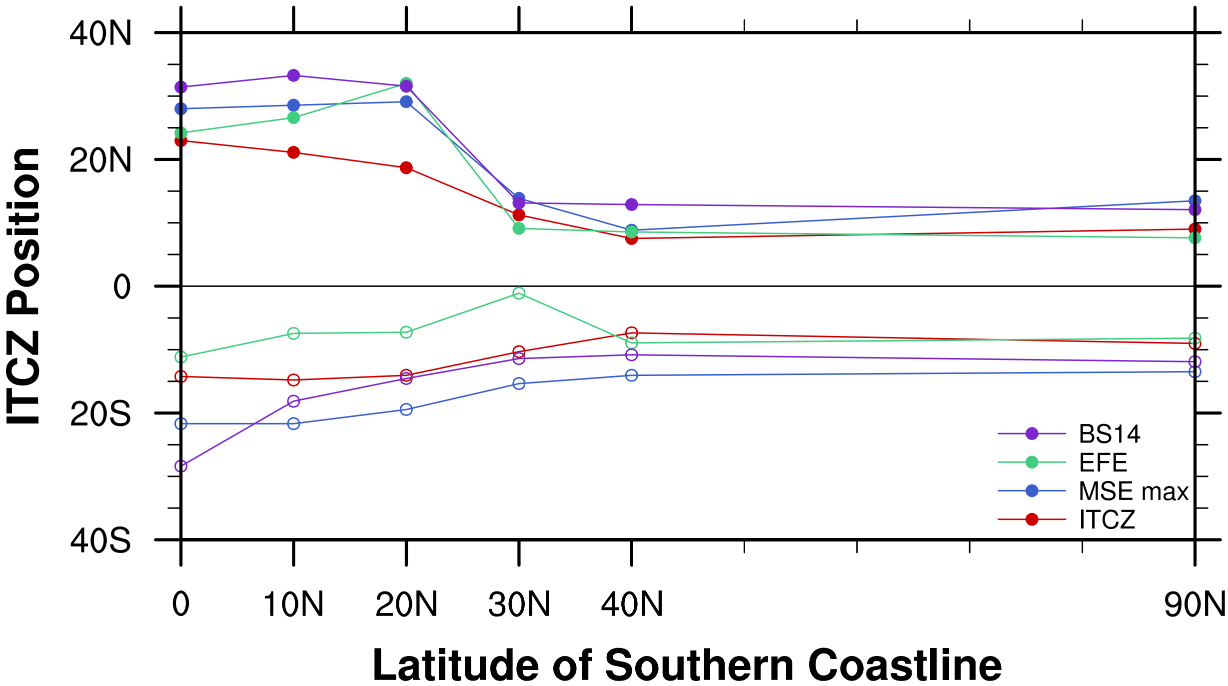

FIG. 8. NH summer (filled circles) and SH summer (open circles) ITCZ position (red), near-surface MSE maximum (blue), EFE (green), and first-order estimate of EFE from BS14 (purple).

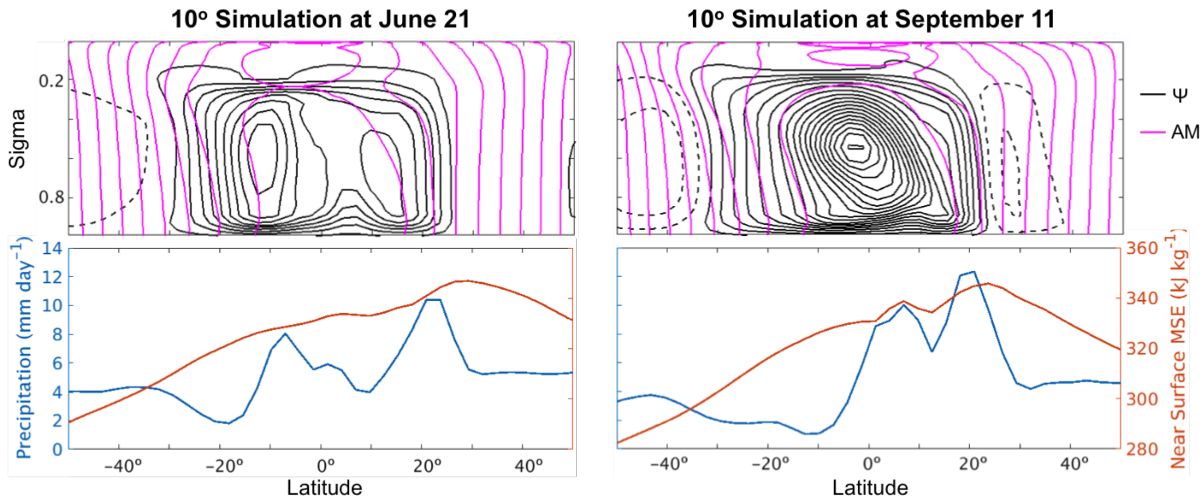

912 FIG. 9.)(Top) Total streamfunction Ψ in black (counterclockwise in solid, clockwise in dashed with contour interval 20×10^9 kg s^{-1}) and angular momentum contours in magenta (contour interval $\Omega a^2/15$) and (bottom) precipitation (blue) and near-surface ($\sigma = 0.887$) MSE distribution (red) from the 10° simulation.

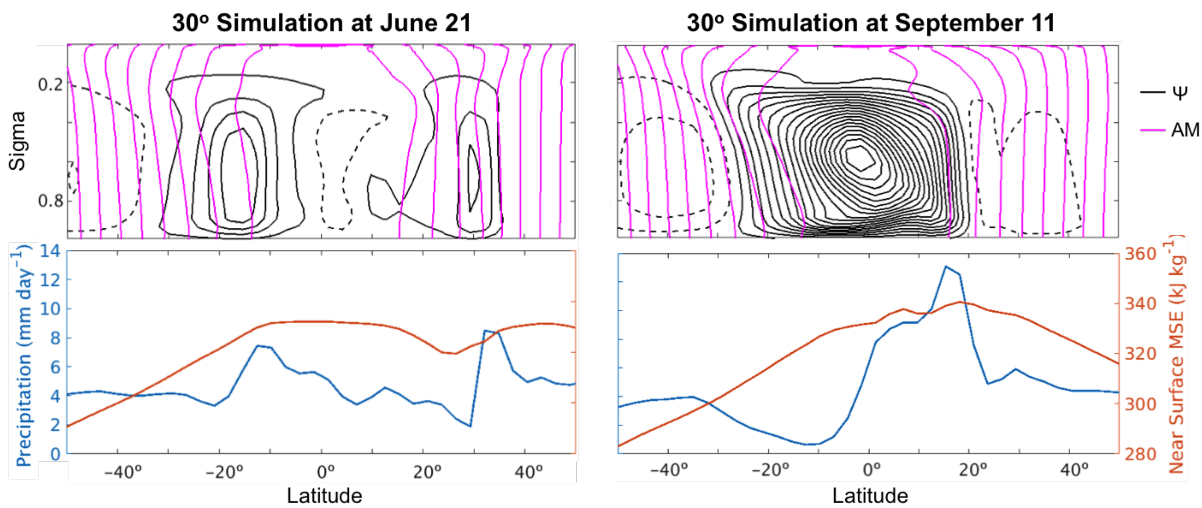

FIG. 10. Same as in Fig. 9 from the 30° simulation.

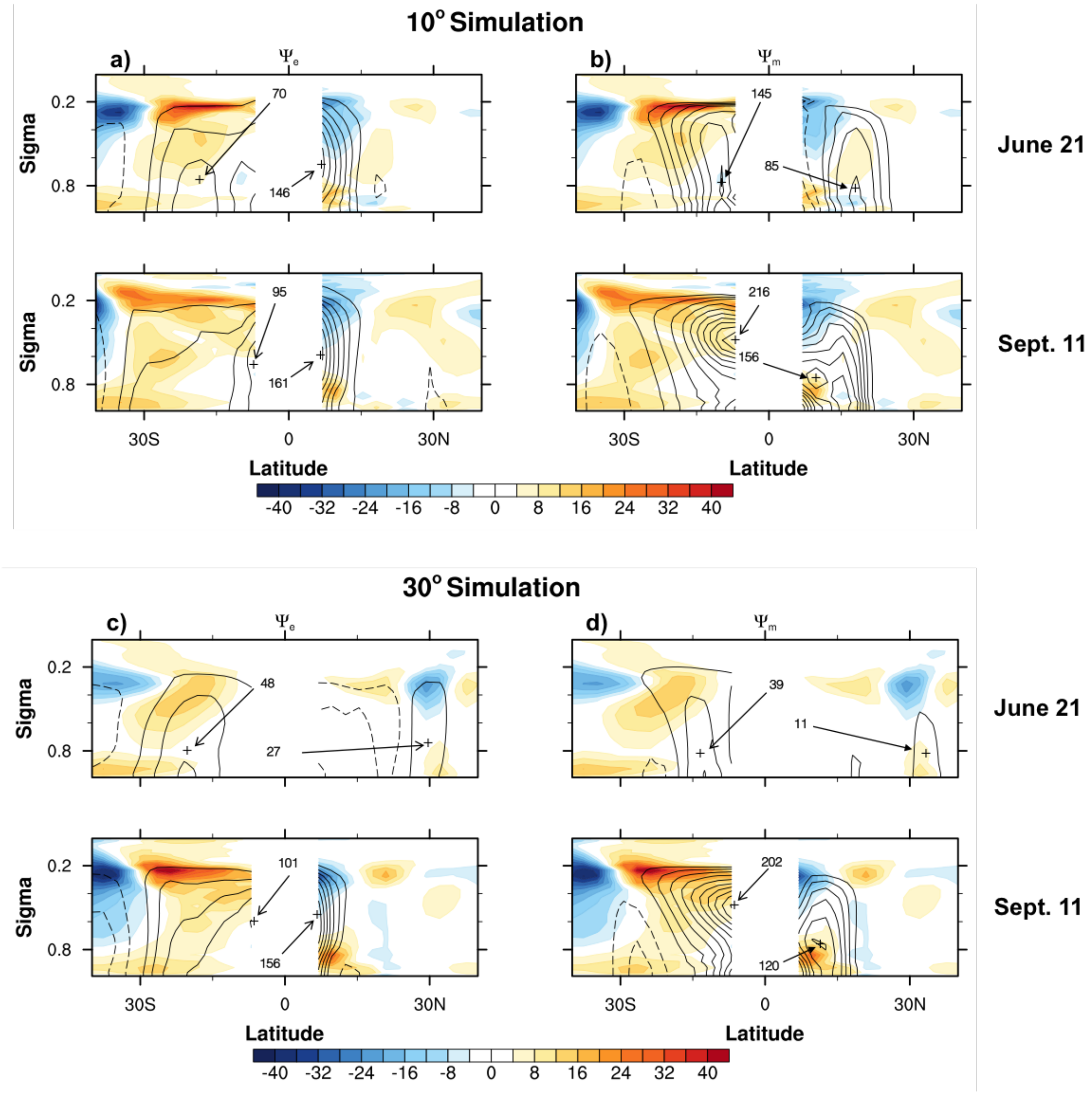

FIG. 11. Decomposition of the total streamfunction Ψ into eddy Ψ_e (left column) and mean Ψ_m (right column) momentum flux components from simulations with southern boundaries of land at 10° (a, b) and 30° (c, d) at June 21 (top) and September 11 (bottom). Ψ_e and Ψ_m are in black contours (counterclockwise in solid, clockwise in dashed with contour interval 20×10^9 kg s^{-1}). The eddy momentum flux divergence is calculated as $-\nabla \cdot (\overline{p}_s \overline{u'v'}^{\sigma} \cos\phi)/\overline{p}_s$, where $\overline{p}_s$ is the zonal and temporal mean surface pressure, $\overline{(\cdot)}^{\sigma}$ is a surface pressure-weighted zonal and temporal mean along sigma surfaces, and $(\cdot)'$ indicates deviations from the mean, and shown in color contour (contour interval 4×10^{-6} m s^{-2}). The NH and SH maxima in both Ψ_e and Ψ_m are given in 10^9 kg s^{-1} and marked by the arrows.

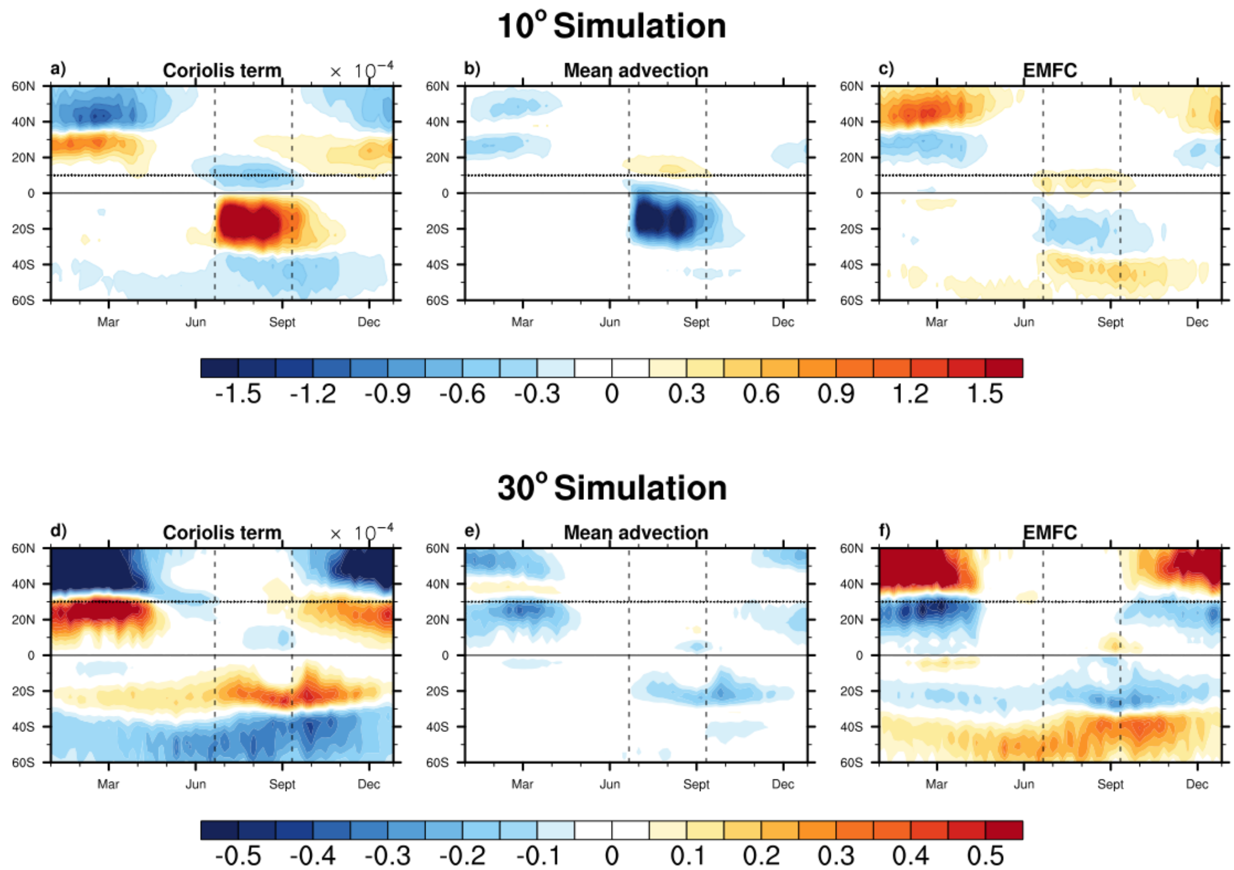

FIG. 12. Seasonal cycle of the terms in the upper-level ($\sigma = 0.195$) zonal momentum budget in Eq. (5): (a) zonal mean Coriolis term $f\overline{v}$, (b) mean flow advection $-(\overline{v}\partial\overline{u}/\partial y + \overline{\omega}\partial\overline{u}/\partial p)$, and (c) transient eddy momentum flux convergence $-(\partial\overline{u'v'}/\partial y+\partial\overline{u'\omega'}/\partial p)$ from the 10° simulation with contour interval 1.5×10^{-5} m s^{-2}, and same terms: (d), (e), and (f), respectively from the 30° simulation with contour interval 0.5×10^{-5} m s^{-2}. Vertical dashed lines mark June 21 and September 11 and the horizontal dotted line represents the continent southern coastline.

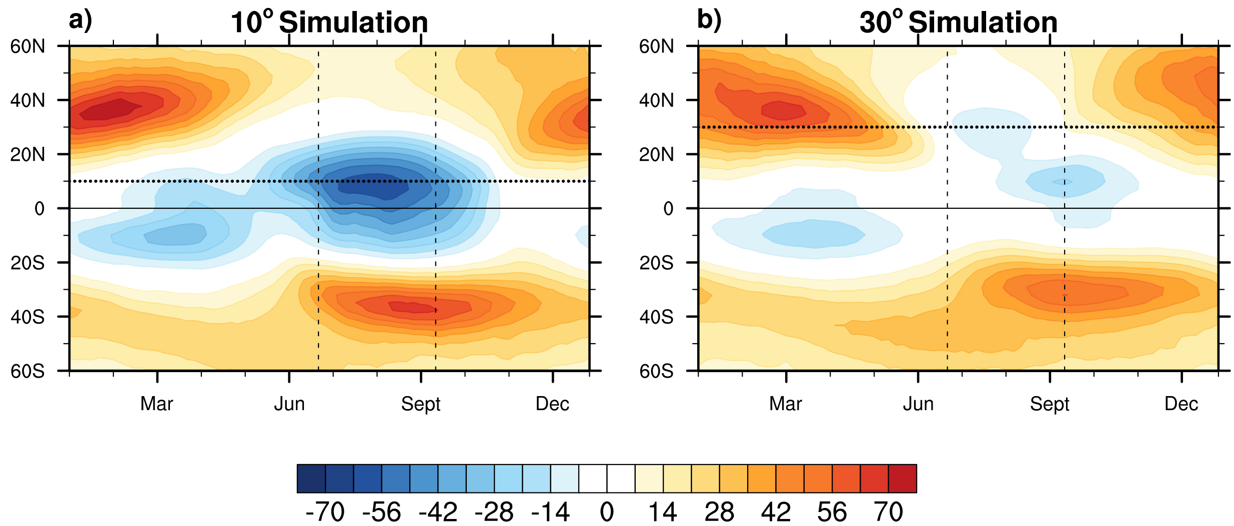

929 FIG. 13. Seasonal cycles of upper-level ($\sigma = 0.195$) zonal wind u_{up} (contour interval 7 m s^{-1}) from the (a)
930 10° and (b) 30° simulations. Vertical dashed lines mark June 21 and September 11 and the horizontal dotted line
931 represents the continent southern coastline.

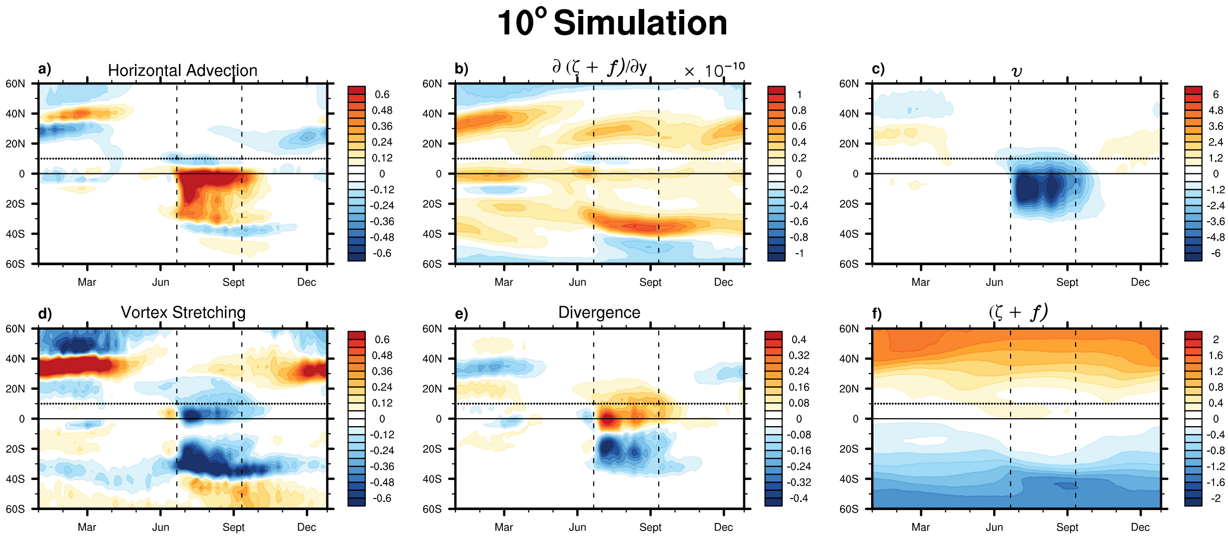

932 FIG. 14. Seasonal cycle and decomposition of terms in the vorticity budget in Eq. (8) from the 10° simulation

933 at $\sigma = 0.195$: (a) $-\mathbf{u}\cdot\nabla(\overline{\zeta}+f)$ (contour interval 0.06 day^{-2}), (b) $\partial(\overline{\zeta}+f)/\partial y$ (contour interval 0.1×10^{-10}

934 m^{-1} s^{-1}), (c) $\overline{v}$ (contour interval 0.6 m s^{-1}), (d) $-(\overline{\zeta}+f)\nabla\cdot\overline{\mathbf{u}}$ (contour interval 0.06 day^{-2}), (e) $\nabla\cdot\overline{\mathbf{u}}$

935 (contour interval 0.04 day^{-1}), and (f) $\overline{\zeta}+f$ (contour interval 0.2 day^{-1}). Vertical dashed lines mark June 21

936 and September 11 and the horizontal dotted line represents the continent southern coastline.

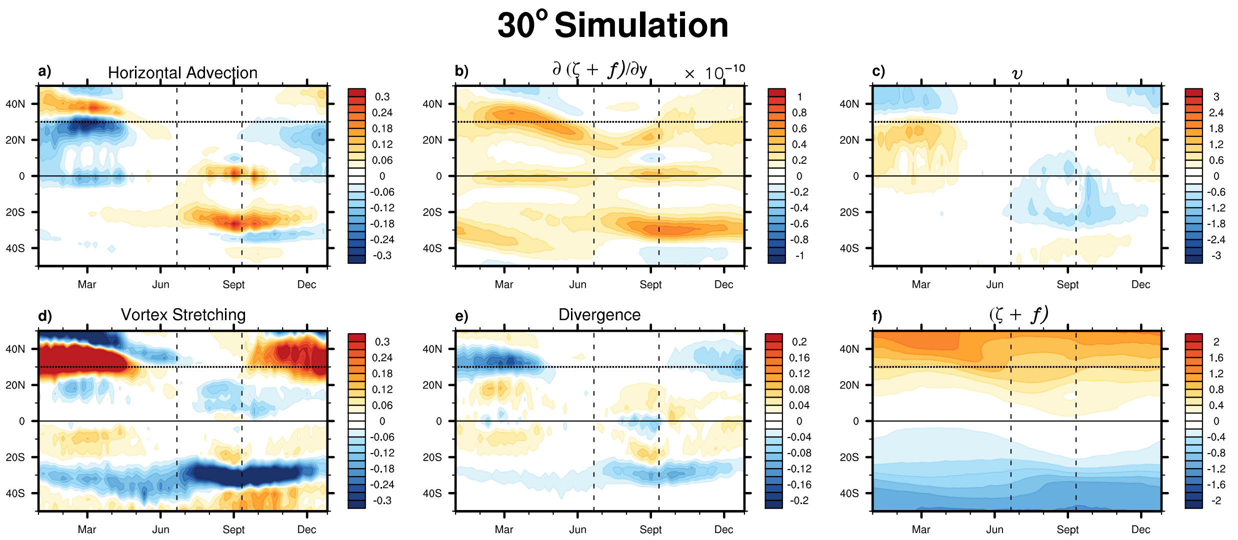

FIG. 15. As in Figure 14, but from the 30° simulation and contour intervals: a) 0.03 day^{-2}, b) 0.1×10^{-10} m^{-1} s^{-1}, c) 0.3 m s^{-1}, d) 0.03 day^{-2}, e) 0.02 day^{-1}, and f) 0.2 day^{-1}.

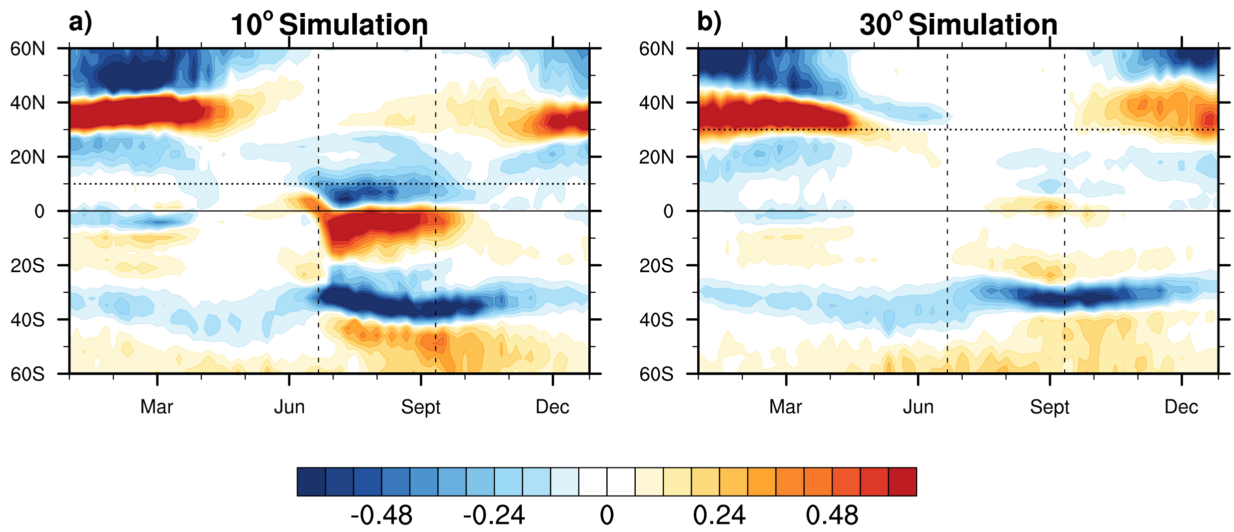

FIG. 16. Total vorticity tendency (sum of the vortex stretching and horizontal advection tendencies from Figs 14 and 15, contour interval 0.06 day^{-2}).